Check for updates

Earthquake Engineering & Structural Dynamics

WILEY

RESEARCH ARTICLE

Shaking Table Tests of a Three-Story Re-Centering Steel Braced Frame with Sliding Slab Connected to Energy Dissipation Devices

Chung-Che Chou[1] | Chi-Jeng Wu[1] | Li-Yu Huang[1] | Alvaro Córdova[1] | Huang-Zuo Lin[2] | Shu-Hsien Chao[2] | Georgios Tsampras[3] | Chia-Ming Uang[3] | Shih-Ho Chao[4] | Hsin-Yang Chung[5]

[1]Department of Civil Engineering, National Taiwan University, Taipei City, Taiwan | [2]National Center for Research on Earthquake Engineering (NCREE), Taipei City, Taiwan | [3]Department of Structural Engineering, University of California, San Diego, California, USA | [4]Department of Civil Engineering, University of Texas, Arlington, Texas, USA | [5]Department of Civil Engineering, National Cheng Kung University, Tainan City, Taiwan

Correspondence: Chung-Che Chou (cechou@ntu.edu.tw)

Received: 21 February 2025 | **Revised:** 11 June 2025 | **Accepted:** 18 August 2025

Funding: This research was supported by the National Science and Technology Council under the project number NSTC 112-2625-M-002-019, Taiwan and the 2022 Innovative Project of National Applied Research Laboratories.

Keywords: friction device | sandwiched buckling-restrained brace | self-centering brace | shaking table test | sliding slab

ABSTRACT

Reducing residual deformation or earthquake loads on the frame structure can enhance its seismic performance during ground motions. This study explores a novel system that uses a self-centering brace (SCB) to provide the re-centering capability of the frame and a sliding slab to reduce the system's acceleration. The floors are allowed to slide with respect to the re-centering steel frame by adding low-friction Teflon sheets, while various horizontal energy dissipating devices are used to enhance the seismic response of the frame. A self-centering disc-spring device is added to re-center the slab after sliding in Phase 1. In addition to the spring device, a friction device in Phase 2 or a steel-only sandwiched buckling-restrained brace in Phase 3 is incorporated. The floor is "rigidly" connected to the frame in Phase 4, simulating a typical frame construction. Four phases, comprising 32 shaking table tests, were conducted on the specimen. A near-fault motion record from the 2022 Guanshan and Chihshang earthquake was used. Phase 1 tests demonstrated that the SCB and horizontal disc-spring device could fully re-center both the frame and sliding slab at the maximum-considered earthquake (MCE) level. In Phases 2 and 3, the addition of horizontal energy dissipating devices to the frame reduced slab movement but resulted in higher floor acceleration compared to Phase 1 tests. Compared to Phase 4, the effect of the sliding slab caused a roof drift reduction of 23% and 18%, and a base shear reduction of 15% and 5%, in Phases 2 and 3, respectively.

1 | Introduction

The slab in a conventional steel structure is rigidly connected to the lateral force-resisting system (LFRS) using shear studs, and no relative movement between the slab and the frame is expected during earthquakes. This research explores the potential of a sliding slab system in a re-centering steel braced frame. The combination of the sliding slab and self-centering brace (SCB) aims to reduce the floor acceleration (i.e., inertial force) and minimize residual deformation of the frame during large earthquakes. Over the last two decades, various SCBs using different technologies have been developed to enhance structural seismic performance through improved damage control [1–8]. Compression-only or tension-only SCBs, which provide seismic force resistance in only

© 2025 John Wiley & Sons Ltd.

Summary

- A new steel system is evaluated by using self-centering brace to provide the re-centering capability of the frame and a sliding slab to reduce the system's acceleration.
- Evaluate the seismic performance by conducting 32 shaking table tests on the full-scale, three-story steel frame in four different phases.
- The sliding slab, equipped with SCSDs in parallel with horizontal energy dissipation devices (i.e., FD or H-SBRB), reduced the seismic force on the frame compared to typical steel frames.
- The residual displacement of the frame specimen with the self-centering brace is very small at an earthquake intensity close to two times the MCE level.

one loading direction, have also been developed to simplify the frame-to-gusset connection details in reinforced concrete (RC) or steel structures [9]. A post-tensioned SCB, developed based on past research works [3, 10], is adopted in this study to provide re-centering capability for the steel frame under earthquake motion. The slab is designed to decouple from the steel braced frame by using Teflon sheets at all precast concrete slab and steel beam interfaces to minimize friction during slab movement. An energy dissipation device, such as a self-centering spring device (SCSD), friction device (FD), or buckling-restrained brace (BRB), is horizontally connected between the slab and the steel beam in the LFRS to limit the inertial force transferred to the LFRS.

Various approaches have been explored to mitigate the seismic response of frames through the development of isolated or energy-dissipated floor systems. Mar and Tipping [11] proposed a story isolation system aimed at reducing base shear and roof acceleration demands. Villaverde et al. [12, 13] introduced a roof isolation system using laminated rubber bearings and viscous dampers, demonstrating reductions in roof drift through numerical simulations and small-scale shake table tests. Cui et al. [14, 15] studied the seismic response of bidirectional spring units in seismically isolated floors, while Liu and Warn [16] examined the sensitivity of the floor system in a steel shear wall structure. Anajafi and Medina [17] explored various parameters influencing the design of multi-floor isolation systems, while Casagrande et al. and Xiang et al. evaluated different types of dampers or materials for isolating selected floors [18, 19]. In addition to isolation systems, a force-limiting connection between the gravity and LFRS has been investigated as an alternative to a rigid connection [20–22]. Zhang et al. [23] further validated the effectiveness of deformable connections through shaking table tests on a four-story RC shear wall building. Paronesso and Lignos [24] incorporated sliding friction dampers and low-damping rubber bearings, showing significant reductions in floor accelerations and drifts in buildings with concentrically braced frames. Chou et al. [25] used all-steel sandwiched buckling-restrained braces (SBRB) or rigid members to connect the sliding floor and the LFRS in a three-story steel dual frame, showing a significant reduction in roof acceleration after the floor slid in shaking table tests. Moreover, Córdova et al. [26] examined the sensitivity of horizontal energy dissipator capacity (i.e., SBRB) in the three-story steel dual frame by conducting nonlinear response history analyses at the design-based earthquake (DBE) and maximum-considered earthquake (MCE) levels.

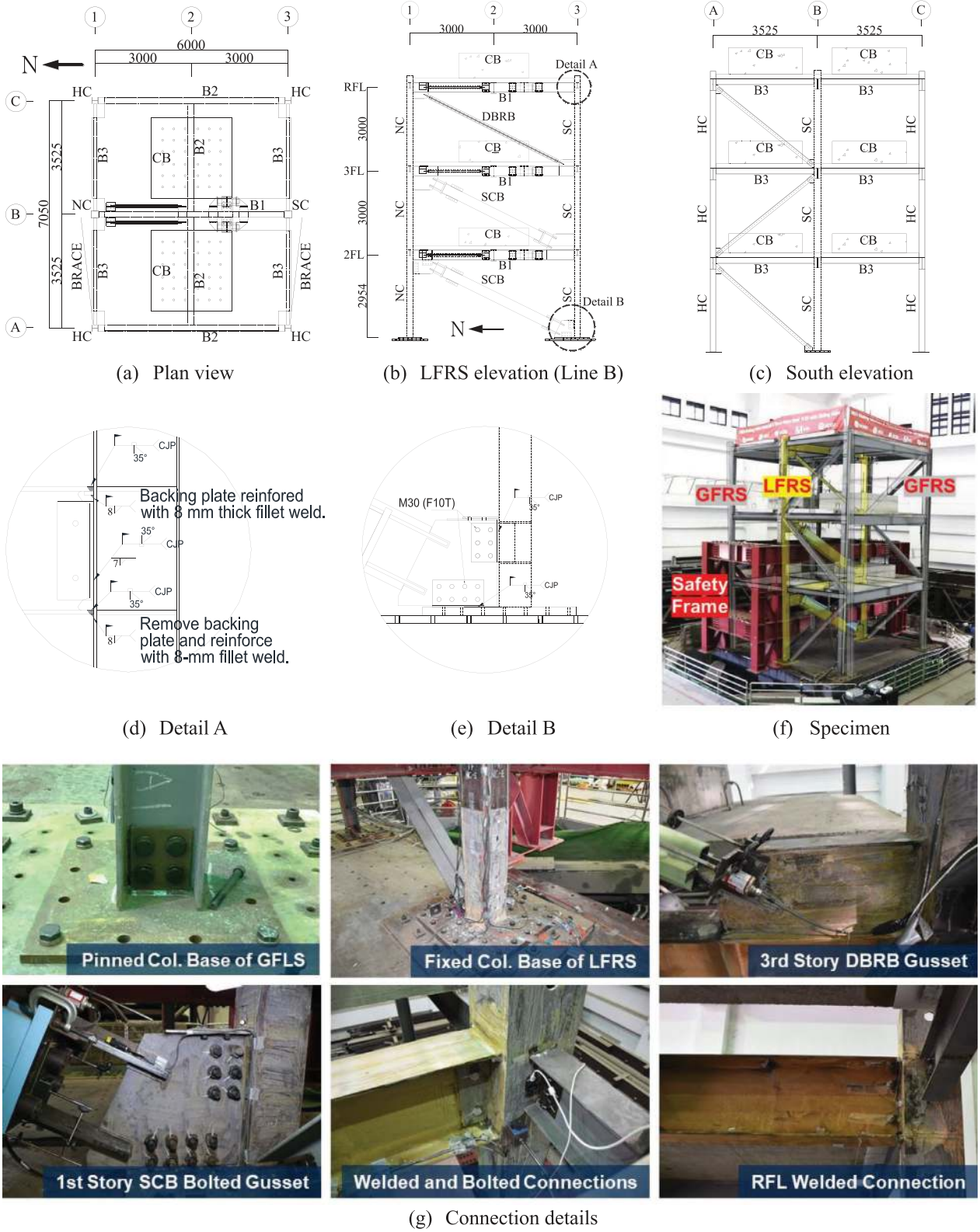
Chou et al. [25] conducted shake table tests on a three-story steel dual frame with a buckling-restrained braced frame (BRBF) that has built-up box columns with b/t ratios complying with the moderately ductile requirement in AISC 341-22 [27]. The column base did not show local buckling nor strength degradation at a motion intensity of about 2.4 × MCE level. The width-thickness (b/t) requirement of the column in a new system with a sliding slab may be relaxed to account for the floor acceleration reduction in earthquakes. To study the seismic performance of the sliding slab and the frame with re-centering properties, shaking table tests were conducted on a full-scale, three-story steel frame. The frame includes an SCB and an SCSD to minimize the residual deformation of the frame and slab, respectively. The frame is also designed with built-up box columns that do not meet the b/t requirement for highly ductile nor moderately ductile members in AISC 341-22 [27]. The frame is equipped with a stiffness-adjustable SCB at the bottom two stories. Each brace consists of three compression members and two sets of tensioning elements in parallel to provide self-centering capability. Disc springs are added to the second core of the SCB to adjust its axial stiffness and deformation capacity to meet the design requirements [10]. Since the brace design force for the SCB at the third story is too small, a diagonal sandwiched buckling restrained brace (D-SBRB) is used to replace the SCB. The SBRB is an all-steel BRB with a steel core, sandwiched by a pair of restraining members without infilled concrete, as verified by past studies [28–30].

The research objective is to evaluate the seismic performance of the re-centering braced frame with sliding slabs and energy dissipation devices used to connect the slab and the frame. Three different horizontal energy dissipation devices are used in this frame specimen in the first three test phases, including SCSDs in Phase 1, FDs in Phase 2, and horizontal all-steel sandwiched buckling-restrained braces (H-SBRB) in Phase 3. The "rigid" connection is provided between the slab and the frame in Phase 4 to study a typical braced frame in the same ground motion. The modification aims to evaluate the effectiveness of the sliding slab by comparing its response to that of a typical frame, as well as to assess the impact of the non-ductile built-up box column on the new frame system. Therefore, the experiment program introduces several novel features compared to previous shaking table tests conducted on self-centering braced frames. It involves a newly developed SCB with post-tensioned tendons and disc springs as the self-centering mechanism, allowing for the adjustment of brace axial stiffness and deformation. Key innovations include: (1) the use of both sliding and conventional slabs within the same steel self-centering braced frame; and (2) the incorporation of horizontal SCSDs and energy dissipation devices (i.e., sandwiched buckling-restrained brace and FD) in different test phases to evaluate their effects on the slab movement and re-centering capability. The results of this study highlight the effectiveness of slab sliding and SCB in enhancing the seismic resilience of steel structures.

10969845, 2025, 15, Downloaded from https://onlinelibrary.wiley.com/doi/10.1002/eqe.70053 by Georgios Tsampras - University Of California , Wiley Online Library on [07/11/2026]. See the Terms and Conditions (https://onlinelibrary.wiley.com/terms-and-conditions) on Wiley Online Library for rules of use; OA articles are governed by the applicable Creative Commons License

2 | Three-Story Steel Braced Frame

The specimen is a full-scale, three-story re-centered braced frame, and shake table tests were conducted along the north-south direction of the frame (Figure 1a). This frame was designed according to a seismic zone III in Taipei, Taiwan [31]. Figure 1a–g shows the plan, elevation, and details of the frame specimen. The LFRS is positioned along Line B of the frame, and the gravity force-resisting system (GFRS) is positioned along Lines A and C of the frame. The LFRS is a braced frame, consisting of stiffness-adjustable SCBs at the bottom two stories and an all-steel D-SBRB at the third story, with cross sections shown in



(a) Plan view (b) LFRS elevation (Line B) (c) South elevation

(d) Detail A (e) Detail B (f) Specimen

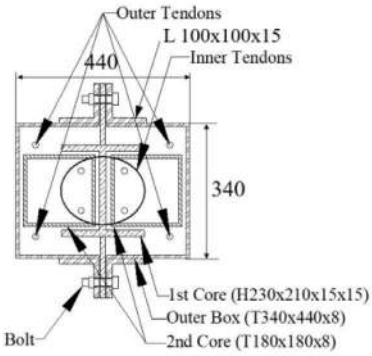
(g) Connection details

FIGURE 1 | Specimen dimensions and details (unit: mm).

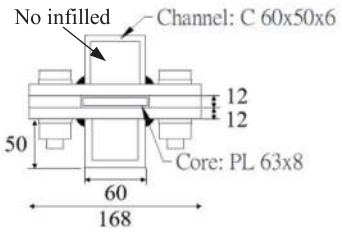
10969845, 2025, 15, Downloaded from https://onlinelibrary.wiley.com/doi/10.1002/eqe.70053 by Georgios Tsampras - University Of California , Wiley Online Library on [07/11/2026]. See the Terms and Conditions (https://onlinelibrary.wiley.com/terms-and-conditions) on Wiley Online Library for rules of use; OA articles are governed by the applicable Creative Commons License



LFRS

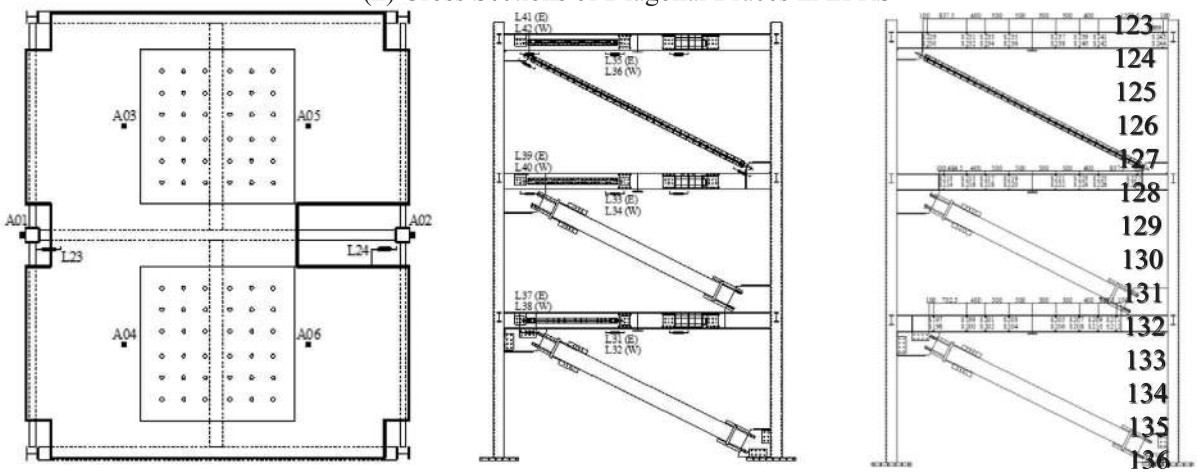


SCB Cross Section (First Story)



SBRB Cross Section (Third Story)

(h) Cross Sections of Diagonal Braces in LFRS



(i) Roof Accelerometer, Displacement Transducer, and Strain Gauge Layout

FIGURE 1 | (Continued)

Figure 1h. Each story has a precast 15 cm-thick concrete slab and two concrete blocks, marked by "CB" in the figure. The total concrete weight is 340, 369, and 413 kN for the second floor, third floor, and roof, respectively. According to Taiwan Seismic Building Code [31], the empirical period of the structure is T_n = 0.26 s. The spectral response acceleration parameter at a short period is S_{DS} = 0.6 g for Taipei site, and the importance factor is I_e = 1.0. The seismic design coefficient, C_s, is 0.196 with the design base shear of 232 kN.

2.1 | LFRS

Table 1 lists dimensions of the beams and columns. All beams and columns are made of SN490B steel with a nominal yield stress of 325 MPa. The SCBs are made of SN490B, and the core of the DBRB is made of SN400 steel with a nominal yield stress of 235 MPa due to a low design force. Table 2 lists test results of steel coupons, where the maximum ratio of the actual yield stress to the nominal yield stress is about 1.35. Since no design guideline of the re-centering steel braced frame is specified in AISC 341-22 [27], all members in the LFRS were designed according to the BRBF provisions in AISC 341-22 [27] and AISC 360-22 [33], except that BRBs were replaced by SCBs of equivalent axial yield strength (activation strength) at the bottom two stories. The

TABLE 1 | Dimensions of beams and columns.

Element	Frame	Section
Column	LFRS (first-3rd story)	NC: box 235 × 235 × 8 (0.9)
		SC: box 235 × 235 × 8 (0.8)
	GFRS (first-3rd story)	HC: H400 × 200 × 8 × 12
Beam	LFRS (2FL-RFL)	B1: H350 × 175 × 7 × 11 (0.7, 1.0, 1.0)
	GFRS (2FL-RFL)	B2: H400 × 200 × 8 × 12
		B3: H200 × 100 × 5.5 × 8

TABLE 2 | Coupon test results.

Material	SN490B						SN400			
Thickness (mm)	7		8		11		6		8	
F_y (MPa)	440	407	371	372	427	425	293	295	297	301
F_u (MPa)	575	553	495	498	555	626	416	418	431	433

10969845, 2025, 15, Downloaded from https://onlinelibrary.wiley.com/doi/10.1002/eqe.70053 by Georgios Tsampras - University Of California , Wiley Online Library on [07/11/2026]. See the Terms and Conditions (https://onlinelibrary.wiley.com/terms-and-conditions) on Wiley Online Library for rules of use; OA articles are governed by the applicable Creative Commons License

beam-to-column moment connection welds (Figure 1d) follow the detailing requirements for the special moment frames in AISC 341-22, while the brace-to-gusset connections (Figure 1g) follow the provisions in AISC 360-22. However, the b/t ratio of the built-up box columns is 27.4, which does not meet the highly ductile member (λ_{hd}) and the moderately ductile member (λ_{md}) requirements in AISC 341-22:

$$\lambda_{hd} = 0.55\sqrt{\frac{E}{R_y F_y}} \tag{1}$$

$$\lambda_{md} = 1.0\sqrt{\frac{E}{R_y F_y}} \tag{2}$$

where using $E = 200$ GPa, $F_y = 325$ MPa, and $R_y = 1.2$ obtains $\lambda_{hd} = 12.5$ and $\lambda_{md} = 22.6$. The initial axial force on the built-up box columns is $0.11P_y$. The beams were welded to the columns using complete joint penetration (CJP) groove welds. The steel backing plate in the beam top flange was retained and reinforced with an 8-mm thick fillet weld. However, the steel backing between the bottom flange of the beam and column was removed, and the root pass was back gouged to sound weld metal before being back welded with an 8-mm reinforcing fillet (as shown in Figure 1d,g). No reduced beam section (RBS) was used in all beams. The design of the SCBs at the bottom two stories was based on the work [10], and the design of the all-steel DBRB at the third story was based on the work [28, 29]. As shown in Figure 1e,g, each end of the first-story SCB was welded to a single gusset plate, which was then bolted to the frame member and the base plate by F10 high-strength bolts, according to the AISC 360-22 [32]. The demand-to-capacity ratios (DCRs) for the columns and beams in the LFRS are also listed in parentheses in Table 1, and DCRs for three diagonal braces are about 0.9.

2.2 | GFRS

The design and configuration of the GFRS in Figure 1f followed the same scheme as in Chou et al. [25]. Table 1 presents the cross-sectional dimensions of the gravity beams B2 and B3 and column HC (H400 × 200 × 8 × 12) shown in Figure 1a,c. The gravity columns were positioned at the four corners of the frame with gravity beams connected in both directions. All the gravity beams were connected to the columns using shear tabs with F10T high-strength bolts to simulate a pin connection, and the gravity columns were pinned to the shake table as well using F10T high-strength bolts, as shown in Figure 1g. The previous shaking table tests conducted on the steel dual frame [25] showed that this configuration, with the partial rotational stiffness of the shear tab, transfers a seismic shear to the GFRS of about 10% of the base shear. The diagonal bracing configuration shown in Figure 1c was designed to provide frame stability in the east-west direction (i.e., out-of-plane stability of the frame).

2.3 | Four Test Phases

Four test phases were conducted on the frame specimen. From Phase 1 to Phase 3, the precast slab was disconnected from all steel beams (i.e., no shear studs used on the beam top flange), and 2 mm-thick Teflon sheets were placed underneath the slab at all slab-to-beam interfaces to minimize friction force during the slab sliding. Additionally, horizontal devices were installed between the slab and the steel beam to mitigate the seismic response of the specimen. The horizontal devices were installed in pairs per slab, one on each side of the steel beam, to avoid force eccentricity to the beam. Different horizontal devices were used to study the effect of slab sliding on the frame response. In Phase 4, a high-stiffness and high-strength member was used to simulate a rigid connection between the slab and the beam as a typical steel frame. Figure 2 shows different horizontal devices in each test phase.

In Phase 1, an SCSD composed of two sets of disc spring stacks, as shown in Figures 2a and 3a was used at each story as a horizontal device to provide the re-centering capability of the sliding slab. Figure 3d shows the corresponding force-displacement relationship of the SCSD before installing to the frame, with a bilinear-elastic and no energy dissipation characteristic [33]. The center part of the SCSD was bolted to the slab and its two ends were bolted to the web of the LRFS beam, as seen in Figure 3a; one of the two disc spring stacks during slab sliding was in compression to provide the re-storing force to the slab. The objectives of this test phase were to reduce the seismic response of the frame by allowing the slab to slide with respect to the frame while minimizing the residual relative displacement of the slab after sliding. In Phase 2, an FD developed at UC San Diego was added to the frame to provide the energy dissipation in addition to the Teflon frictional energy, as shown in Figure 2b. In this case, the slab can move relative to the beam with the capability of SCSD self-centering and additional FD energy dissipation. Figure 3b shows the schematic of the FD, and Figure 3e shows the corresponding force-displacement relationship. In Phase 3, the FD was replaced by the horizontal all-steel sandwiched buckling-restrained brace (H-SBRB) at each story, as shown in Figure 2c. Figure 3c shows a sketch of the H-SBRB, and Figure 3f shows the corresponding force-displacement relationship before installation to the frame. One end of the FD or H-SBRB was connected to the slab, and the other end was connected to the beam web of the LFRS. The effect of different energy dissipation devices on the floor and frame response can be studied from the test results of Phase 1 to Phase 3. In Phase 4, all horizontal devices were replaced by a high-strength and high-stiffness structural tee member to simulate a rigidly-connected floor in a typical steel frame, as shown in Figure 2d.

3 | Design Force of Horizontal Energy Dissipation Device

Figure 4a shows the mechanism of the sliding slab at each floor, where $u_{s,i}$ is the slab displacement, $u_{f,i}$ is the frame displacement, and $u_{rel,i}$ is the relative displacement between the slab and the frame:

$$u_{s,i} = u_{f,i} + u_{rel,i}\ i = 2FL,\ 3FL,\ RFL \tag{3}$$

Under the assumption that the elastic deformation of the steel members connecting the horizontal device to the steel frame is negligible relative to the deformation of the horizontal device, $u_{rel,i}$ is equal to the deformation of the horizontal device. The force equilibrium is obtained from the free body diagram (FBD), as

10969845, 2025, 15, Downloaded from https://onlinelibrary.wiley.com/doi/10.1002/eqe.70053 by Georgios Tsampras - University Of California , Wiley Online Library on [07/11/2026]. See the Terms and Conditions (https://onlinelibrary.wiley.com/terms-and-conditions) on Wiley Online Library for rules of use; OA articles are governed by the applicable Creative Commons License

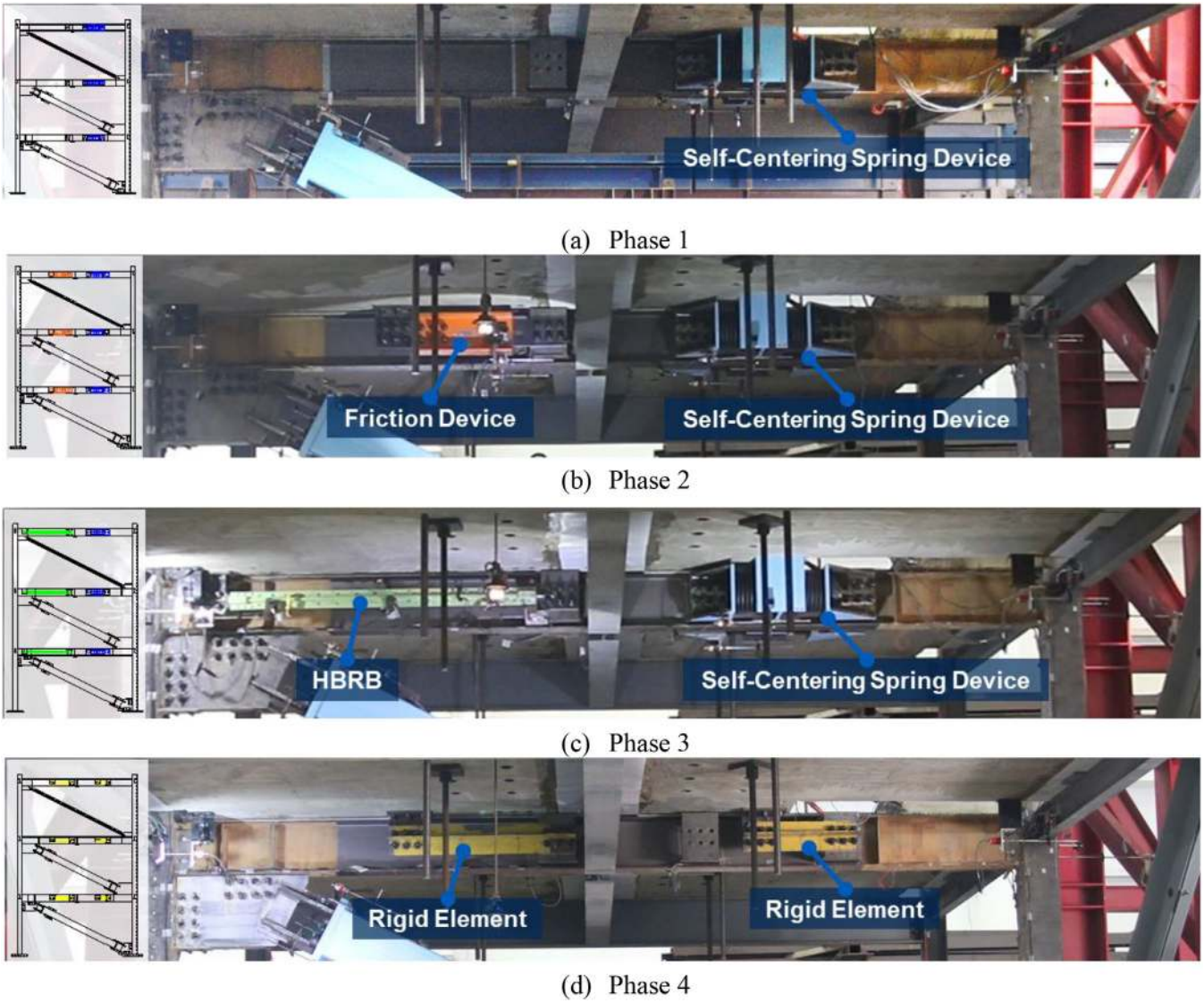


FIGURE 2 | Horizontal energy dissipating devices between the slab and beam in four test phases.

shown in Figure 4b,c:

$$\begin{cases} F_{in,i} = 2F_{SCSD,i} + F_{f,i} \ \ (Phase\ 1) \\ F_{in,i} = 2F_{SCSD,i} + 2F_{device,i} + F_{f,i} \ \ (Phases\ 2\ and\ 3) \end{cases} \quad (4)$$

where $F_{in,i}$ is the floor inertial force, $F_{SCSD,i}$ is the axial force of the SCSD, $F_{device,i}$ is the axial force of the horizontal device, and $F_{f,i}$ is the friction force developed at the interface between the steel beam and the slab.

In a conventional building construction, the diaphragm force in ASCE 7-22 [34] is amplified by the system overstrength factor (i.e., $\Omega_o = 2.5$ for a dual frame system with BRBF) to design connectors between the slab and the frame, preventing yielding during the maximum considered earthquake (MCE) level. Cordova et al. [26] developed a three-dimensional (3D) model of the three-story dual frame by correlating shaking table test results of Chou et al. [25]. Nonlinear response history analyses were conducted on the frame and showed that when using the design force per ASCE 7-22, the slab sliding could occur at the DBE level. Therefore, this study adopts the design force in ASCE 7-22 [34] to design the horizontal devices:

$$F_{px} = \frac{\sum_n^{i=x} F_i}{\sum_n^{i=x} w_i} w_{px} \quad (5)$$

where F_i is the floor force in Section 12.8.3 of the ASCE 7-22, and w_{px} and w_i are the floor weight. In addition, Equation (5) should be larger than $0.2S_{DS}I_e w_{px}$ and lower than $0.4S_{DS}I_e w_{px}$. These thresholds are associated with 0.5 and 1.0 times the peak ground acceleration (PGA) multiplied by the floor mass (w_{px}), respectively. The code recommends that the design floor acceleration should exceed at least 0.5 times the PGA.

For the purpose of designing the horizontal device, the inertial force in Equation (4), $F_{in,i}$, is set to be the diaphragm force, F_{px}, in Equation (5). Table 3 lists the floor weight, w_{px}, and the diaphragm force, F_{px}, at each floor, x. In Phase 1 tests, only two SCSDs were used to connect the slab and the frame. Consequently, the diaphragm force was distributed to the SCSDs and the Teflon-steel friction mechanism. The Teflon-steel interface has a friction coefficient that depends on the relative velocity between the slab

10969845, 2025, 15, Downloaded from https://onlinelibrary.wiley.com/doi/10.1002/eqe.70053 by Georgios Tsampras - University Of California , Wiley Online Library on [07/11/2026]. See the Terms and Conditions (https://onlinelibrary.wiley.com/terms-and-conditions) on Wiley Online Library for rules of use; OA articles are governed by the applicable Creative Commons License

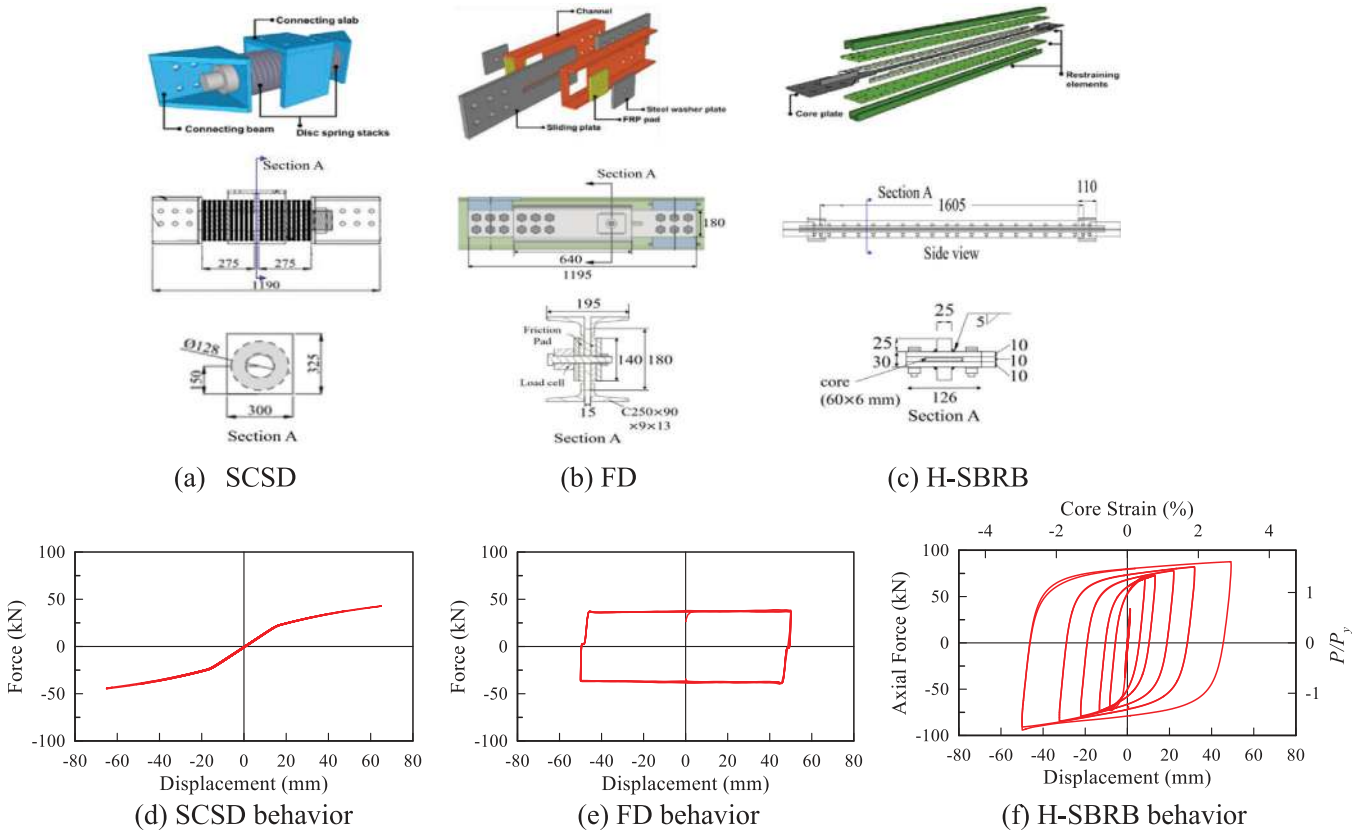


FIGURE 3 | SCSD, FD, and H-SBRB used in this study and their corresponding force–deformation relationships.

TABLE 3 | Design force of horizontal energy-dissipating device.

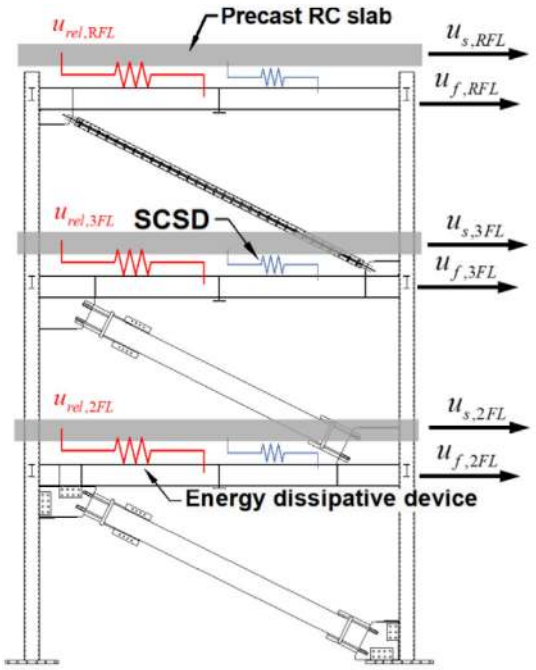
Floor	w_{px} (kN)	F_{px} (kN)	$F_{f,i}$ (kN)	Phase 1 $F_{SCSD,i}$ (kN)	Phase 2 $F_{SCSD,i}$ (kN)	Phase 2 $F_{FD,i}$ (kN)	Phase 3 $F_{SCSD,i}$ (kN)	Phase 3 $F_{H\text{-}SBRB,i}$ (kN)	Phase 4 Tee Member Force (kN)
RF	413	100	41	30 (1.1)	3	27 (0.7)	3	27 (0.7)	125 (0.5)
3F	369	88	37	26 (1.0)	3	23 (0.6)	3	23 (0.6)	110 (0.4)
2F	340	70	34	18 (0.7)	3	15 (0.8)	3	15 (0.8)	88 (0.3)

and the beam. According to Córdova et al. [26], the coefficient increased rapidly to approximately 0.1 for low relative velocities, up to about 10 mm/s, and continued to increase at a much slower rate as the velocity increased. Therefore, this value was used to calculate the Teflon-steel friction force at the design level, $F_{f,i}$ listed in Table 3, by multiplying the coefficient and the floor weight, w_{px}. The Teflon friction force, $F_{f,i}$, was subtracted from the diaphragm force, and then divided by two to obtain the design force for one SCSD. Figure 4d is a flowchart, presenting a design procedure for horizontal devices at each floor. For example, the diaphragm force and the Teflon friction force at the roof are F_{pRF} = 100 kN and $F_{f,RF}$ = 41 kN (=0.1 × 413) from Steps 1 and 2, respectively, and a design force for one SCSD is $F_{SCSD,i}$ = 30 kN because of two SCSDs per floor. The design force of the spring, F_{act}, represents the force at a stiffness transition point between the initial elastic stiffness, K_1, and the post-elastic stiffness, K_2, of the bilinear spring device (Figure 3d), being $F_{act} = F_{SCSD,i}$ in Step 3. To configure the SCSD, the stiffness of a single disc spring, K_{ds}, is determined to be 8.46 kN/mm based on component tests in [33]. As shown in Figure 3a, the spring assembly consists of n_s = 20 springs in series and n_p = 1 in parallel, resulting in a device length of 1190 mm, suitable for the erection between the steel beam and the slab. The loading stiffness of the disc spring stack is given by ${K_{stack}}^{l} = K_{ds}(n_p/n_s) = 0.423$ kN/mm in Step 4. The unloading stiffness of the stack, ${K_{stack}}^{u2}$, is approximately half the loading stiffness from [33], resulting in ${K_{stack}}^{u2} = 0.212$ kN/mm. In the frame, the SCSD force, F_{act}, is transferred by the center plate of the device from the slab, as shown in Figures 2a and 3a, and then distributed to both ends of the SCSD connecting to the beam. The corresponding pre-compression force, F_{ds}, is determined by [33]:

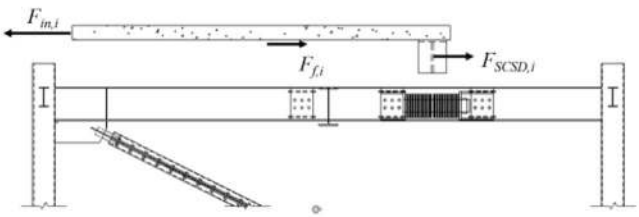
$$F_{ds} = F_{act}\frac{{K_{stack}}^{l}}{{K_{stack}}^{l} + {K_{stack}}^{u2}} \tag{6}$$

The required pre-compression force of a single disc spring is F_{ds} = 19 kN, which is also equal to the pre-compression force of the

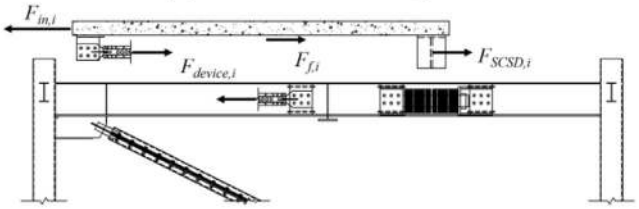
10969845, 2025, 15, Downloaded from https://onlinelibrary.wiley.com/doi/10.1002/eqe.70053 by Georgios Tsampras - University Of California , Wiley Online Library on [07/11/2026]. See the Terms and Conditions (https://onlinelibrary.wiley.com/terms-and-conditions) on Wiley Online Library for rules of use; OA articles are governed by the applicable Creative Commons License



(a) Kinematics



(b) FBD of the sliding slab in Phase 1



(c) FBD of a sliding slab in Phases 2 and 3

Phase 1

Step 1: Compute the diaphragm force F_{px} using Eq. (5) in accordance with ASCE 7-22 [34].

Step 2: Calculate the Teflon friction force at each floor based on [26]:

$$F_{f,i} = 0.1 \times w_{px}$$

where w_{px} is the weight of floor x.

Step 3: Determine the design force for the SCSD:

$$F_{SCSD,i} = \frac{F_{px} - F_{f,i}}{n}$$

where n is the number of SCSD per floor. Then, define the yield force (i.e., force at the stiffness change) of the SCSD as:

$$F_{act} = F_{SCSD,i}$$

Step 4: Compute the precompression force of one disc spring using Eq. (6) based on [33]:

$$F_{ds} = F_{act}\frac{K_{stack}{}^{l}}{K_{stack}{}^{l} + K_{stack}{}^{u2}}$$

where $K_{stack}{}^{l}=K_{ds}(n_p/n_s)$, K_{ds}=8.46 kN/mm from disc spring component tests in [33], n_p is the number of springs in parallel, n_s is the number of springs in series, and $K_{stack}{}^{u2} = K_{stack}{}^{l}/2$.

Step 5: Using a configuration of disc springs and solving for the displacement of one disc spring, δ_{ds}, using Eq. (7) [35]:

$$F_{ds} = \frac{4E}{1-\mu^2}\frac{t'^4}{M_1 {D_e}^2}{M_4}^2\frac{\delta_{ds}}{t'}\left[{M_4}^2\left(\frac{h_0'}{t'}-\frac{\delta_{ds}}{t'}\right)\left(\frac{h_0'}{t'}-\frac{\delta_{ds}}{2t'}\right)+1\right]$$

Step 6: Compute the total displacement of the SCSD as $\delta_{in} = \delta_{ds} n_s$, and obtain the initial stiffness of the SCSD as $K_1 = F_{act}/\delta_{in}$.

Phases 2 and 3

Step 7: Compute the yield displacement of the H-SBRB, Δ_y, based on the core length, L_c, the core yield stress, F_y, and the young's modulus of steel, E. Then, determine the force of the SCSD when the H-SBRB yields:

$$F_{SCSD,i} = K_1 \Delta_y$$

where K_1 is the initial stiffness of the SCSD as determined from Step 6 in Phase 1 procedure.

Step 8: Using the same Teflon friction force as in Step 2, compute the H-SBRB force at each floor:

$$F_{device,i} = F_{H-SBRB,i} = \frac{F_{px} - F_{f,i}}{n} - F_{SCSD,i}$$

where n is the number of H-SBRBs per floor. Use this force and a strength reduction factor of 0.9 for designing the H-SBRB (or FD).

(d) Design Flowchart

FIGURE 4 | Mechanism of the sliding slab system and design flowchart.

10969845, 2025, 15, Downloaded from https://onlinelibrary.wiley.com/doi/10.1002/eqe.70053 by Georgios Tsampras - University Of California , Wiley Online Library on [07/11/2026]. See the Terms and Conditions (https://onlinelibrary.wiley.com/terms-and-conditions) on Wiley Online Library for rules of use; OA articles are governed by the applicable Creative Commons License

spring stack due to all springs in a series configuration. Then, the displacement δ_{ds} corresponding to F_{ds} is computed based on [35] in Step 5:

$$F_{ds} = \frac{4E}{1-\mu^2}\frac{t'^4}{M_1 {D_e}^2} {M_4}^2 \frac{\delta_{ds}}{t'} \times \left[{M_4}^2 \left(\frac{{h_0}'}{t'} - \frac{\delta_{ds}}{t'} \right) \left(\frac{{h_0}'}{t'} - \frac{\delta_{ds}}{2t'} \right) + 1 \right] \quad (7)$$

where each disc spring has an inner diameter D_i = 127 mm, outer diameter D_e = 250 mm, and thickness t' = 6.7 mm. The geometry-dependent spring constants are M_1 = 0.69 and M_4 = 1.03, the free cone height of the disc spring is h_0' = 8.1 mm, and the material properties of the steel are E = 200 GPa and μ = 0.3. Solving for the pre-compression displacement of one disc spring, δ_{ds} = 1.3 mm, results in a total displacement of the SCSD of $\delta_{in} = \delta_{ds} n_s = 26\ mm$. With F_{act} and δ_{in} known, the initial stiffness of the SCSD is computed to be $K_1 = F_{act}/\delta_{in}$ = 1.2 kN/mm in Step 6, close to 1.5 kN/mm from the SCSD test [33]. Given that the roof is expected to experience the largest force than bottom two stories, and to facilitate the construction process, the same SCSD used at the roof is adopted for the second and third floors.

In Phase 3 tests, the SCSDs were connected in parallel with the H-SBRBs. Since the elastic stiffness of H-SBRBs is expected to be significantly larger than that of SCSDs, a larger portion of the diaphragm force is distributed to H-SBRBs, assuming the slab as a rigid body in earthquake motion. The yield displacement of the H-SBRB is calculated as $\Delta_y = F_y L_c/E$ = 2 mm, where the nominal yield stress is F_y = 235 MPa, the BRB core length is L_c = 1756 mm, and the Young's modulus is E = 200 GPa. At the displacement level, the force in the SCSD is $F_{SCSD} = K_1 \Delta_y = (1.5)(2) = 3$ kN in Step 7. The same Teflon-friction force used for designing SCSDs in Phase 1 is applied in Phase 3 to obtain the H-SBRB design force in Step 8. The same procedure is adopted for designing the FD in Phase 2. The DCRs for each device are also listed in parentheses in Table 3. The design force for the structural tee member is amplified by 2.5 from F_{px} at each floor to simulate a "rigid" connection between the slab and the beam.

4 | Four Test Phases

Shaking table tests were conducted at the Tainan laboratory, National Center for Research on Earthquake Engineering (NCREE). Figure 1i shows the instrumentation layout, including accelerometers and displacement transducers used to measure the floor and frame acceleration, relative displacement between the floor and slab, and horizontal brace movement at each floor level. In addition to the displacement transducer, an optical motion capture system with 118 sensors was used to measure the movement of the floor, column, and shaking table. A total of 343 strain gauges were used to measure strains in the beams, columns, diagonal braces, and horizontal devices. Fourteen load cells were used to measure bolt load variations in the FDs and SCBs.

The selected ground motion was obtained from the September 18, 2022, Guanshan and Chihshang Earthquake, recorded in the East-West direction at National Yuli Senior High School (Station code EYUL), close to a collapsed building [36]. Figure 5 shows the recorded acceleration history in the East-West direction. Several tests were conducted with different intensities by scaling the PGA. Table 4 lists the test sequence for each phase and presents the test intensity by normalizing the PGA of the table to the design PGA at the DBE level (=0.24 g) and MCE level (=0.32 g). Six tests were conducted in Phase 1, and eight tests were conducted in Phases 2 and 3, where the first six had similar intensities as in Phase 1. Ten tests were conducted in Phase 4, where the first eight tests had similar intensities to the previous test phases. A white noise test with a maximum intensity of 0.015 g was conducted after each test to obtain the structural period of the frame specimen using the Covariance-Driven Stochastic Subspace Identification (SSI-COV) method of Mrabet et al. [37]. Table 4 shows the initial fundamental period of the frame T_n = 0.38–0.39 s, in each phase, indicating that the frame specimen can retain its elastic stiffness after each test phase. Figure 6 shows the acceleration response spectra with a damping ratio of 0.05 for all tests based on the recorded table acceleration time history, and the code spectra at the DBE and MCE levels are also shown for comparison. Note that the maximum response spectrum value occurs near the initial fundamental period of the frame specimen.

Phase 1 was terminated after Test 6 (1.1 × MCE level) due to the maximum displacement limitation of the SCSD. Test 6 had the same intensity level as Test 5 but the motion direction was reversed to minimize the residual relative displacement between the slab and the frame for the following tests in other phases. In Phases 2 and 3, the specimen was tested with two additional tests (Tests 7 and 8), where Test 8 had the same acceleration intensity as Test 7 but the motion direction was reversed for the same purpose as in Test 6, Phase 1. In this case, the minor residual relative displacement between the slab and the frame at the end of Phase 2 facilitated the dismantling of all FDs and the installation of HBRBs. Likewise, at the end of Phase 3, the test sequence

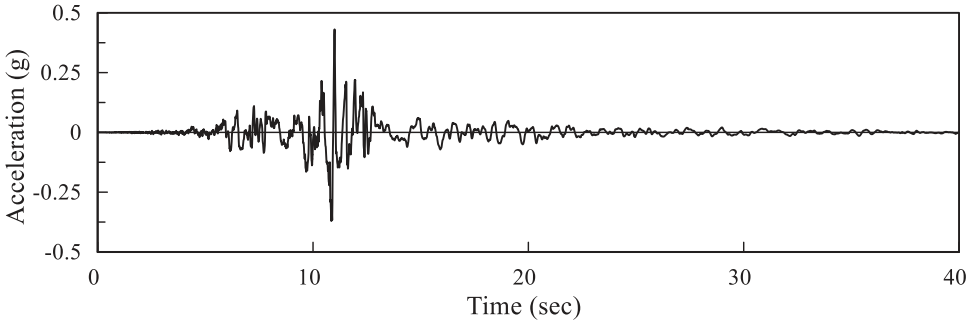


FIGURE 5 | Input ground motion at EYUL station in East-West direction (no scaled).

10969845, 2025, 15, Downloaded from https://onlinelibrary.wiley.com/doi/10.1002/eqe.70053 by Georgios Tsampras - University Of California , Wiley Online Library on [07/11/2026]. See the Terms and Conditions (https://onlinelibrary.wiley.com/terms-and-conditions) on Wiley Online Library for rules of use; OA articles are governed by the applicable Creative Commons License

TABLE 4 | Test intensity and maximum drift in all tests.

Test No.	PGA (g)	Test intensity	Peak roof drift (mm) [drift angle (×0.01 rad)]	Residual roof drift (mm) [drift angle (×0.01 rad)]	Period (s)
(a) Phase 1					
1	−0.02	0.06 × DBE	5.1 [0.06]	0.2 [0.00]	0.39
2	−0.08	0.35 × DBE	10.3 [0.11]	−0.02 [0.00]	0.39
3	−0.19	0.81 × DBE	19.6 [0.22]	−1.4 [−0.02]	0.46
4	0.23	0.94 × DBE	26.0 [0.29]	−2.0 [−0.02]	0.37
5	0.35	1.1 × MCE	25.1 [0.28]	−3.2 [−0.04]	0.42
6	−0.35	−1.1 × MCE	−35.6 [−0.40]	−2.6 [−0.03]	0.42
(b) Phase 2					
1	−0.02	0.06 × DBE	7.8 [0.09]	−3.1 [−0.03]	0.38
2	−0.08	0.35 × DBE	−8.7 [−0.10]	−4.4 [−0.05]	0.44
3	−0.17	0.7 × DBE	26.4 [0.29]	−1.9 [−0.02]	0.44
4	−0.22	0.92 × DBE	38.4 [0.43]	0.2 [0.00]	0.41
5	−0.32	0.98 × MCE	45.8 [0.51]	0.7 [0.01]	0.42
6	0.38	−1.2 × MCE	−54.3 [−0.60]	−3.4 [−0.04]	0.42
7	0.53	1.66 × MCE	63.3 [0.70]	−1.4 [−0.02]	0.43
8	−0.51	−1.61 × MCE	−74.8 [−0.83]	−6.9 [−0.08]	0.42
(c) Phase 3					
1	−0.02	0.06 × DBE	1.6 [0.02]	−6.9 [−0.08]	0.39
2	−0.08	0.35 × DBE	7.4 [0.08]	−6.6 [−0.07]	0.41
3	−0.19	0.81 × DBE	21.2 [0.24]	−6.9 [−0.08]	0.44
4	−0.25	1.05 × DBE	34.0 [0.38]	−6.1 [−0.07]	0.42
5	−0.33	1.03 × MCE	48.8 [0.54]	−4.1 [−0.05]	0.40
6	0.34	−1.05 × MCE	−61.0 [−0.68]	−4.2 [−0.05]	0.44
7	0.45	1.42 × MCE	88.2 [0.98]	−2.5 [−0.03]	0.39
8	−0.48	−1.48 × MCE	−98.5 [−1.09]	−8.4 [−0.09]	0.45
(d) Phase 4					
1	−0.02	0.06 × DBE	1.8 [0.02]	−7.6 [−0.08]	0.38
2	−0.08	0.35 × DBE	−8.4 [−0.09]	−7.5 [−0.08]	0.39
3	−0.19	0.81 × DBE	−22.9 [−0.25]	−9.6 [−0.11]	0.41
4	−0.25	1.04 × DBE	37.2 [0.41]	−9.2 [−0.10]	0.43
5	−0.33	1.02 × MCE	59.5 [0.66]	−6.7 [−0.07]	0.44
6	0.35	−1.1 × MCE	−64.9 [−0.72]	−5.6 [−0.06]	0.42
7	−0.43	1.35 × MCE	64.0 [0.71]	−0.9 [−0.01]	0.47
8	0.46	−1.44 × MCE	−117.1 [−1.30]	−13.2 [0.15]	0.38
9	0.61	1.89 × MCE	160.5 [1.78]	1.3 [0.01]	0.46
10	−0.56	−1.76 × MCE	−174.4 [−1.94]	−18.2 [−0.20]	0.40

also facilitated the dismantling of HBRBs and the installation of structural tee members.

5 | Shaking Table Test Results of Frame Specimen

Figure 7 shows the displacement history of the frame specimen at the roof in Phases 1 to 4. In Phase 1, the steel frame peak roof drift angle was 0.0028 rad and 0.004 rad in Tests 5 and 6 at the intensity level of 1.1 × MCE. The reason for the different roof drift angle is because the frame specimen had a residual roof drift angle of −0.0004 rad at the end of Test 5, and given that Test 6 had a reversed direction, giving more frame drift in the negative direction. In Phase 2, the peak roof drift angle was 0.008 rad in Test 8 (1.6 × MCE level), but in Test 8 (1.5 × MCE level) of Phase 3, the specimen reached a larger peak roof drift angle of

10969845, 2025, 15, Downloaded from https://onlinelibrary.wiley.com/doi/10.1002/eqe.70053 by Georgios Tsampras - University Of California , Wiley Online Library on [07/11/2026]. See the Terms and Conditions (https://onlinelibrary.wiley.com/terms-and-conditions) on Wiley Online Library for rules of use; OA articles are governed by the applicable Creative Commons License

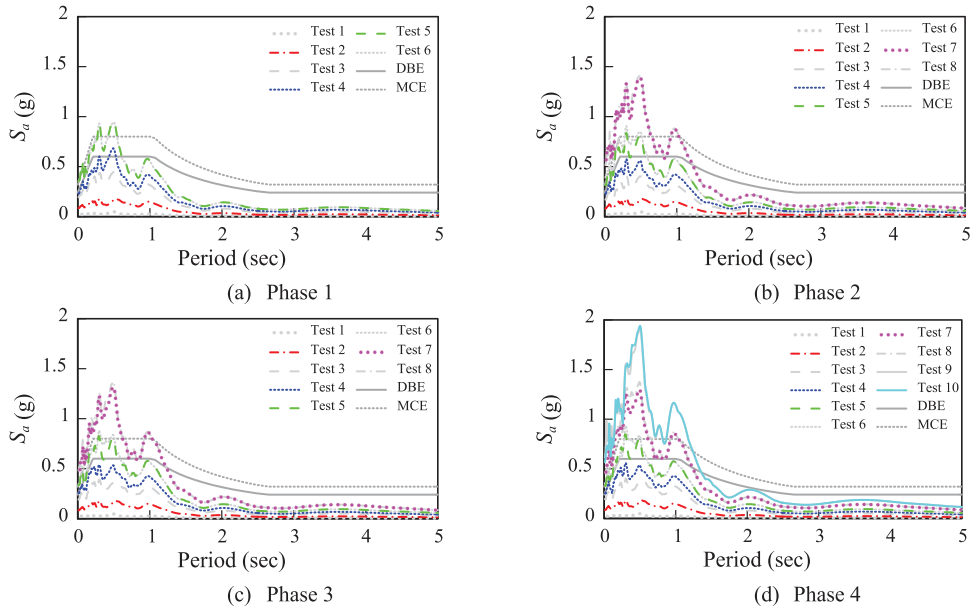


FIGURE 6 | Response spectra of all tests.

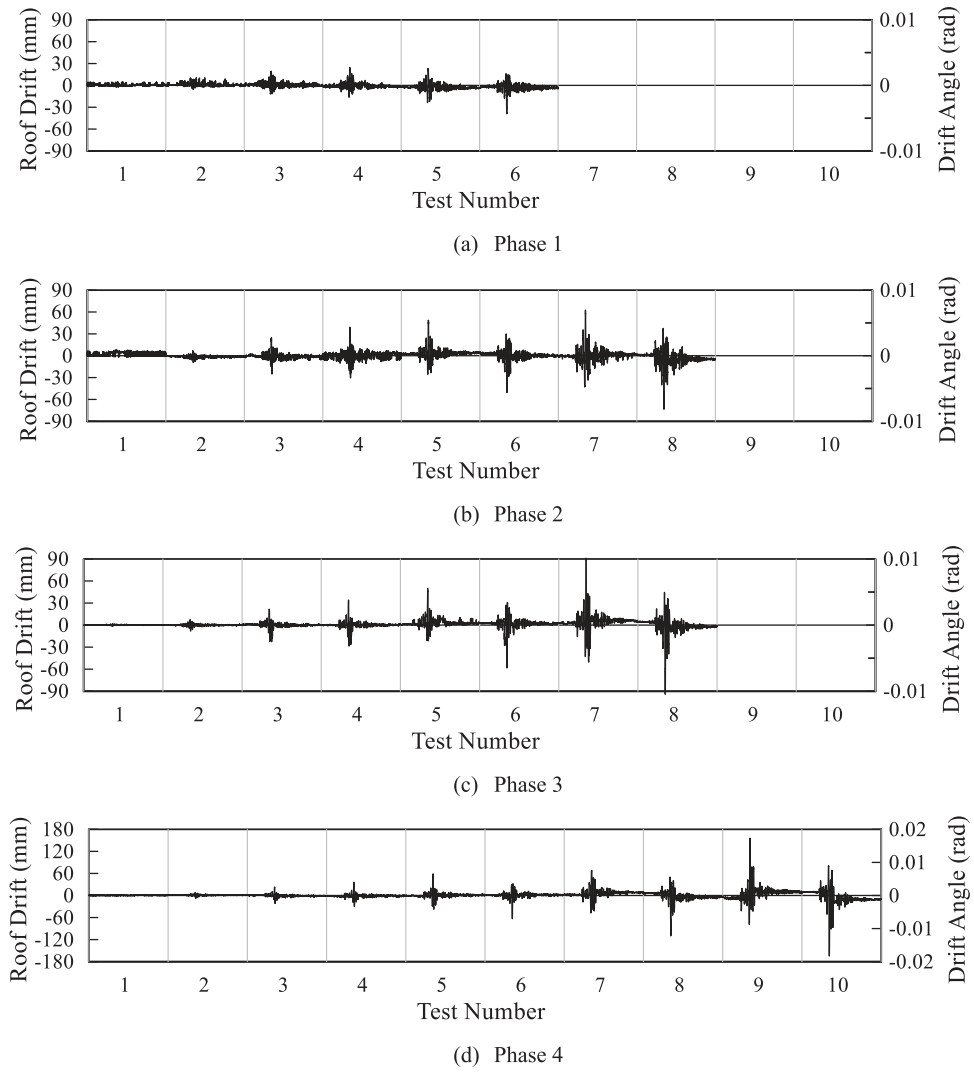


FIGURE 7 | Displacement history of the frame specimen at the roof.

10969845, 2025, 15, Downloaded from https://onlinelibrary.wiley.com/doi/10.1002/eqe.70053 by Georgios Tsampras - University Of California , Wiley Online Library on [07/11/2026]. See the Terms and Conditions (https://onlinelibrary.wiley.com/terms-and-conditions) on Wiley Online Library for rules of use; OA articles are governed by the applicable Creative Commons License

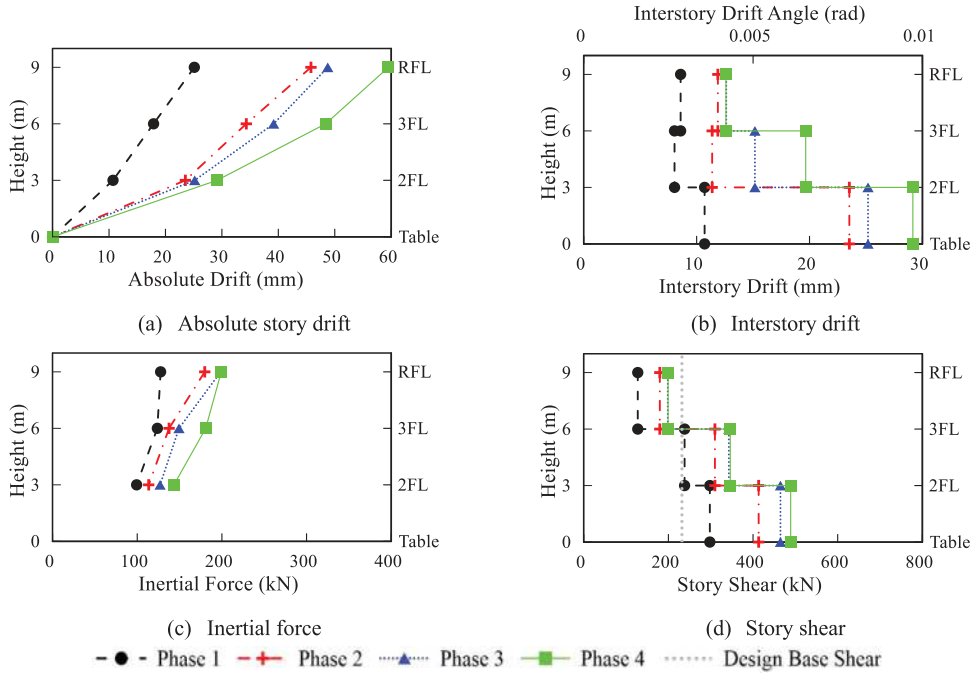


FIGURE 8 | Peak frame drift and story shear in Test 5 (MCE level).

0.01 rad, which was slightly lower than that in Phase 2. The largest recorded residual roof drift in Test 8 of Phase 3 was below a drift angle of 0.001 rad. In Phase 4, the specimen reached a peak roof drift angle of 0.019 rad with a very minor residual drift angle of 0.002 rad after all tests. In general, the residual drift of the frame was minimal due to the effectiveness of SCBs at the bottom two stories when comparing the test response of the steel dual frame with BRBs under the same motion [25].

Figure 8 shows the peak frame drift and story shear in Test 5 (MCE level) for four phases. Figure 8a shows the peak absolute frame drift response, u_{fi}. As expected, the figure shows a response governed by a typical first-mode shape of the braced frame because of its low-rise structural characteristic. The frame had the smallest drift in Phase 1 (only with SCSD), followed by Phases 2 (with SCSD and FD) and Phase 3 (with SCSD and H-SBRB). Figure 8b shows the interstory drift of the frame, where the maximum interstory drift was observed at the first story in all phases. Likewise, the frame in Phase 1 showed the lowest interstory drift compared to that in Phases 2–4. The peak interstory drift at the first story was reduced by 63%, 19%, and 14% in Phases 1, 2, and 3, respectively, when compared to Phase 4 test result. Figure 8c,d shows the inertial force and story shear distribution along the frame height. The shear at the first story was reduced by 39%, 15% and 5% in Phases 1, 2, and 3, when compared to Phase 4 test result. The observation showed that the inclusion of the sliding slab in the frame resulted in a reduction of both frame drift and force responses. Figure 9a,b show the interstory drift and the story shear in Tests 4, 5, 7, and 9 in only Phase 4. In Test 4 (DBE level), the peak interstory drift at the first story was 0.0054 rad, and the base shear was 351 kN, exceeding the design base shear of 232 kN. In Test 9, the peak interstory drift at the first story was 0.024 rad, and the base shear was 791 kN, which was about 3.4 times the design base shear. Although the first-story interstory drift of the frame was large, its residual interstory drift was 0.002 rad (Figure 9c). From Figure 7 and Table 4, the maximum residual drift angle of the roof is 0.0003, 0.0008, 0.0009, 0.002 rad in Phases 1–4, respectively, indicating that even during 1.9 × MCE level test (Phase 4), no repair is needed for the three-story re-centering braced frame even with a rigidly connected slab-to-frame system [34, 38]. The minor residual inter-story drifts were induced by the yielding of the braces, beams, and column base in Phase 4. In addition, nonlinear time history analyses were performed on three steel single-bay steel frames equipped with SCBs and BRBs under near-field motions [2]. For the low- to mid-rise re-centering braced frame, the average peak inter-story drift of the frames under motions with a PGA of 0.4 g was about 0.01 rad, close to the values observed in Tests 5–7 (PGA = 0.33–0.43 g) in Phase 4 (see Figure 9c). The results suggest that the design of the re-centering steel braced frame—originally based on the BRBF approach and implemented by substituting BRBs with SCBs of equivalent yield (or activation) strength—may benefit from modifications that account for different hysteretic behaviors of SCBs and BRBs.

5.1 | Sliding Slab Response

The slab was able to slide relative to the steel frame in Phases 1 to 3. Figure 10a,b shows the sliding displacement of the roof slab in Test 5 (MCE level) and Test 7 (1.4–1.7 times MCE level). Sliding of the slab exhibits a significant pulse response due to a pulse-like input ground motion. Figure 10c shows the peak roof relative displacement of the slab in each test. The slab was activated to slide in Test 3, Phase 1, with a peak relative displacement of 11 mm. When the energy dissipating device was installed with the SCSD in Phases 2 and 3, the slab sliding was activated in Test 4 (DBE level) with a peak relative displacement of 9 and 3 mm in Phases 2 and 3, respectively. As the motion intensity increased, the slab sliding also increased, reaching a maximum

10969845, 2025, 15, Downloaded from https://onlinelibrary.wiley.com/doi/10.1002/eqe.70053 by Georgios Tsampras - University Of California , Wiley Online Library on [07/11/2026]. See the Terms and Conditions (https://onlinelibrary.wiley.com/terms-and-conditions) on Wiley Online Library for rules of use; OA articles are governed by the applicable Creative Commons License

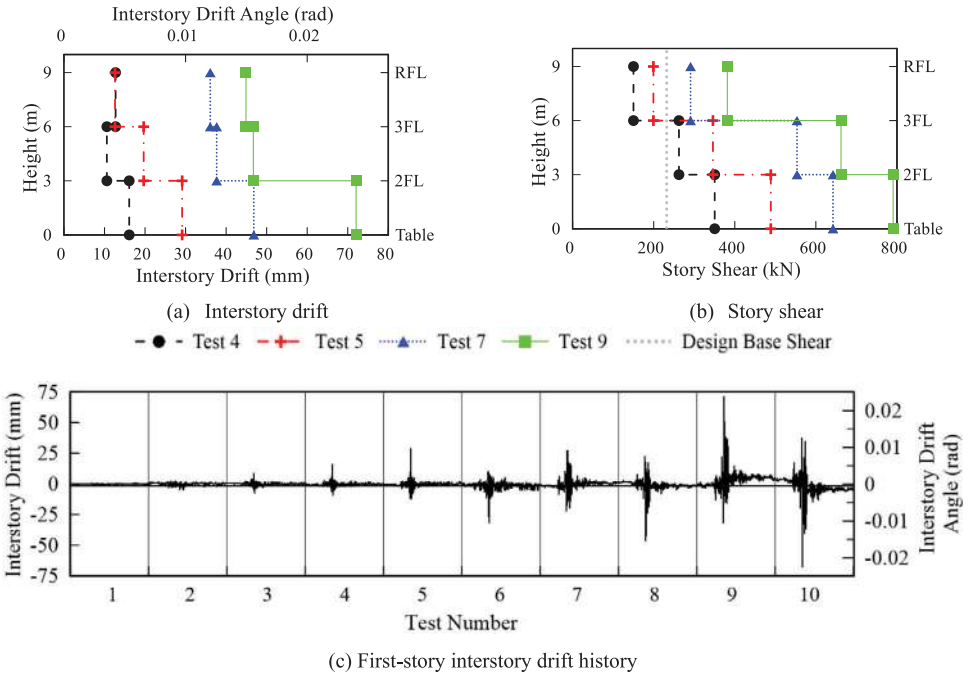


FIGURE 9 | Interstory drift and story shear in only Phase 4 tests.

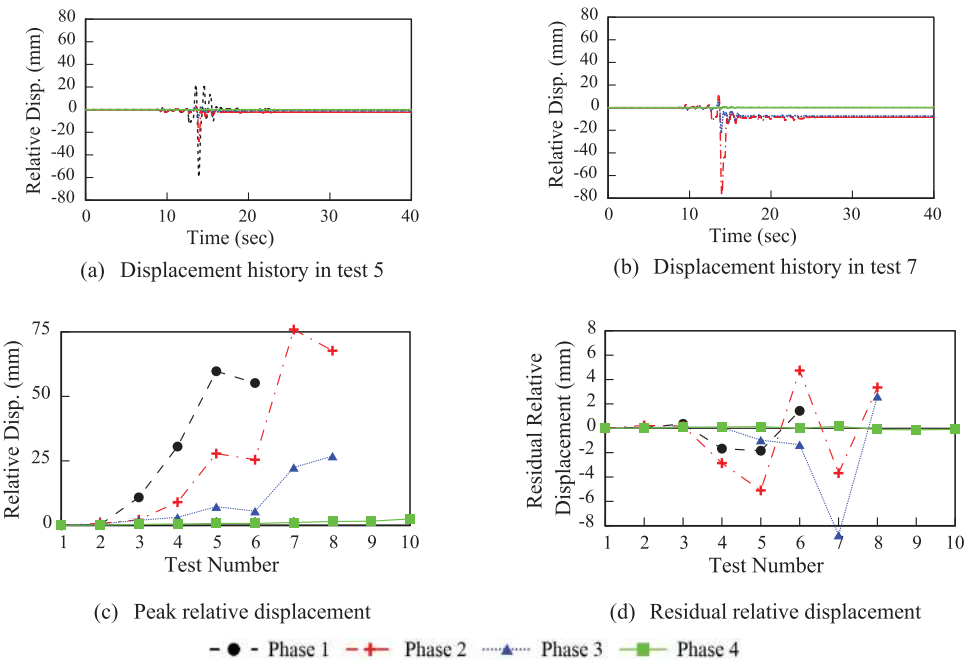


FIGURE 10 | Peak relative displacement and residual relative displacement at the roof for all phases.

value in Tests 7 or 8 of Phases 2 and 3. At the MCE level (Test 5), the maximum roof relative displacement was 60 mm in Phase 1, much larger than 28 and 7 mm in Phases 2 and 3. Therefore, the addition of energy dissipation devices, such as the FD or H-SBRB, significantly reduce the slab sliding. The slab relative displacement is further decreased for the frame specimen with H-SBRB than with FD due to the post-yield stiffness of H-SBRB, unlike FD, in the hysteretic response (Figure 3e,f). As the slab movement increases, the frame displacement decreases, as shown in Figure 8b. In Phases 2 and 3, the combined resistance of the H-SBRB (or FD) with SCSDs is larger than that of the SCSDs alone in Phase 1, causing more forces to be transferred to the frame and resulting in a larger drift. In Phase 4, the maximum relative displacement is below 3 mm in Tests 9 or 10 (1.9 × MCE level), verifying the effectiveness of the structural tee member for simulating a "rigid" connection between the slab and the beam.

Figure 10d shows the roof residual relative displacement of the slab after each test. No residual displacement of the slab is observed throughout tests in Phase 4. When the slab is connected

10969845, 2025, 15, Downloaded from https://onlinelibrary.wiley.com/doi/10.1002/eqe.70053 by Georgios Tsampras - University Of California , Wiley Online Library on [07/11/2026]. See the Terms and Conditions (https://onlinelibrary.wiley.com/terms-and-conditions) on Wiley Online Library for rules of use; OA articles are governed by the applicable Creative Commons License

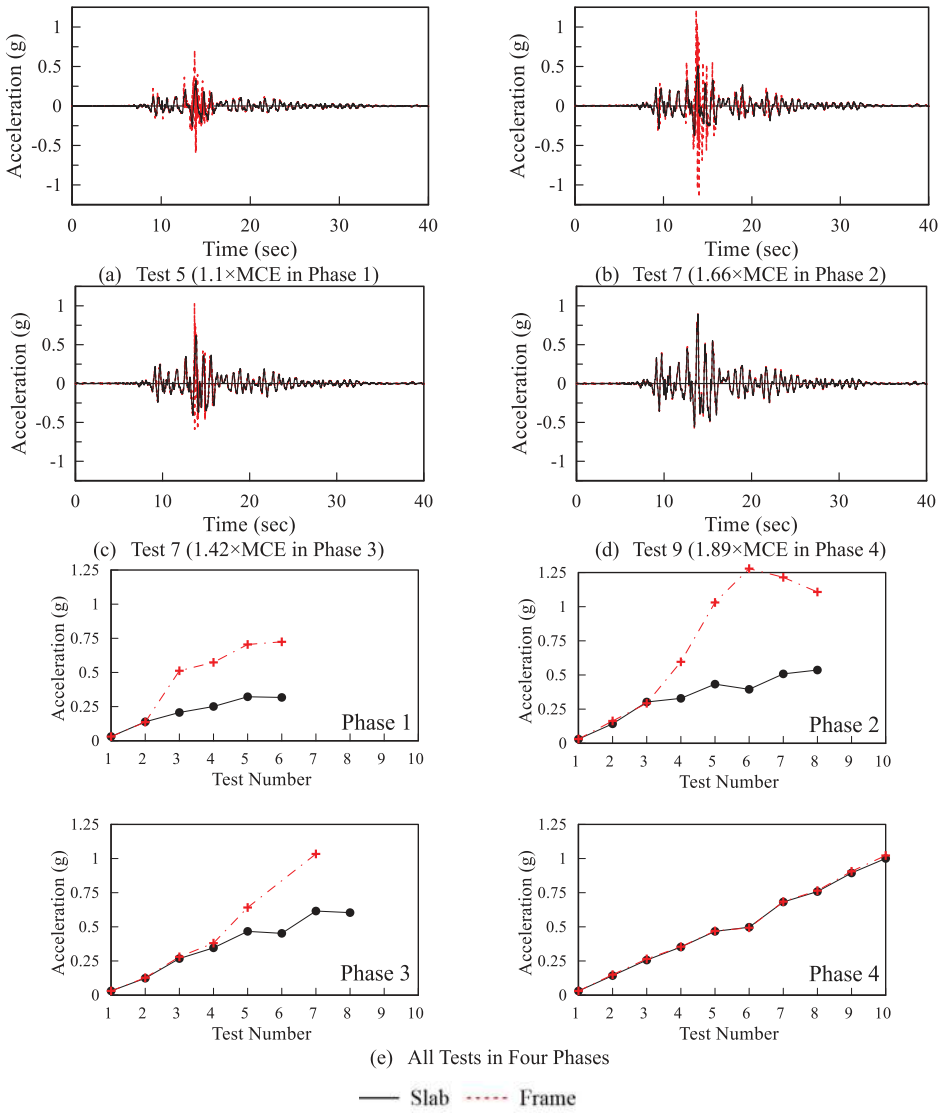


FIGURE 11 | Slab and frame acceleration history and peak acceleration at roof.

to the beam with only SCSD in Phase 1 tests, the maximum residual relative displacement of the slab is 2 mm after sliding 60 mm in Tests 5 or 6 (MCE level), demonstrating the re-centering capability of the slab with SCSDs. Adding H-SBRB can even decrease the slab residual displacement before Test 6 (1.2 times MCE level) in Phase 3, not the case in Phase 2 with FD. Once the H-SBRB experienced large axial deformation, its resting condition (i.e., zero force) at the end of the test had a large permanent deformation because its axial force is larger than the restoring force of SCSD (Figure 3d,f), decreasing the re-centering capability of the slab at Test 7 (1.4–1.7 times MCE level). Figure 11a–d shows the slab and frame acceleration histories at the roof. The reduction of floor acceleration is clear in the first three phases due to slab sliding, particularly at the time t = 14 s, which is associated with a peak relative displacement. In Phase 4, the acceleration history of the slab is similar to that of the frame, indicating that the structural tee members effectively connected the slab and the frame together. Figure 11e shows the peak acceleration of the slab and frame at all tests. Reduction of floor acceleration starts at Test 3 in Phase 1 and Test 4 in Phases 2 and 3, corresponding to the 0.8 × DBE to DBE level (see Table 4). Greater floor acceleration reductions are observed at MCE level (Test 5) or higher earthquake intensity levels in Phases 1–3. In contrast, Phase 4, which represents a conventional floor system, does not exhibit such reductions.

For comparison purposes, the peak acceleration on the roof slab was normalized by that on the table, as shown in Figure 12a. Compared to tests in Phase 4 (i.e., rigidly-connected slab), more slab acceleration reduction was observed in Phase 1 than in Phases 2 and 3 due to larger slab relative displacement, as shown in Figure 10c. In Test 5 (MCE level), the slab acceleration decreased by 36%, 3.7%, and 1.1% in Phases 1, 2, and 3, respectively, when compared to Phase 4 test. The slab acceleration reduction in Phases 2 and 3 became clear after Test 5, when the slab had a large relative displacement. In Tests 7 or 8 of Phases 2 and 3, a more significant slab sliding results in more reduction in slab acceleration (i.e., 36% and 16%, respectively). The slab acceleration reduction also affects the inertial force reduction, as shown in Figure 8c, indicating the importance of slab sliding in the system. It is worth highlighting that the slab inertial force increased in Phases 2 and 3 compared to Phase 1, due

10969845, 2025, 15, Downloaded from https://onlinelibrary.wiley.com/doi/10.1002/eqe.70053 by Georgios Tsampras - University Of California , Wiley Online Library on [07/11/2026]. See the Terms and Conditions (https://onlinelibrary.wiley.com/terms-and-conditions) on Wiley Online Library for rules of use; OA articles are governed by the applicable Creative Commons License

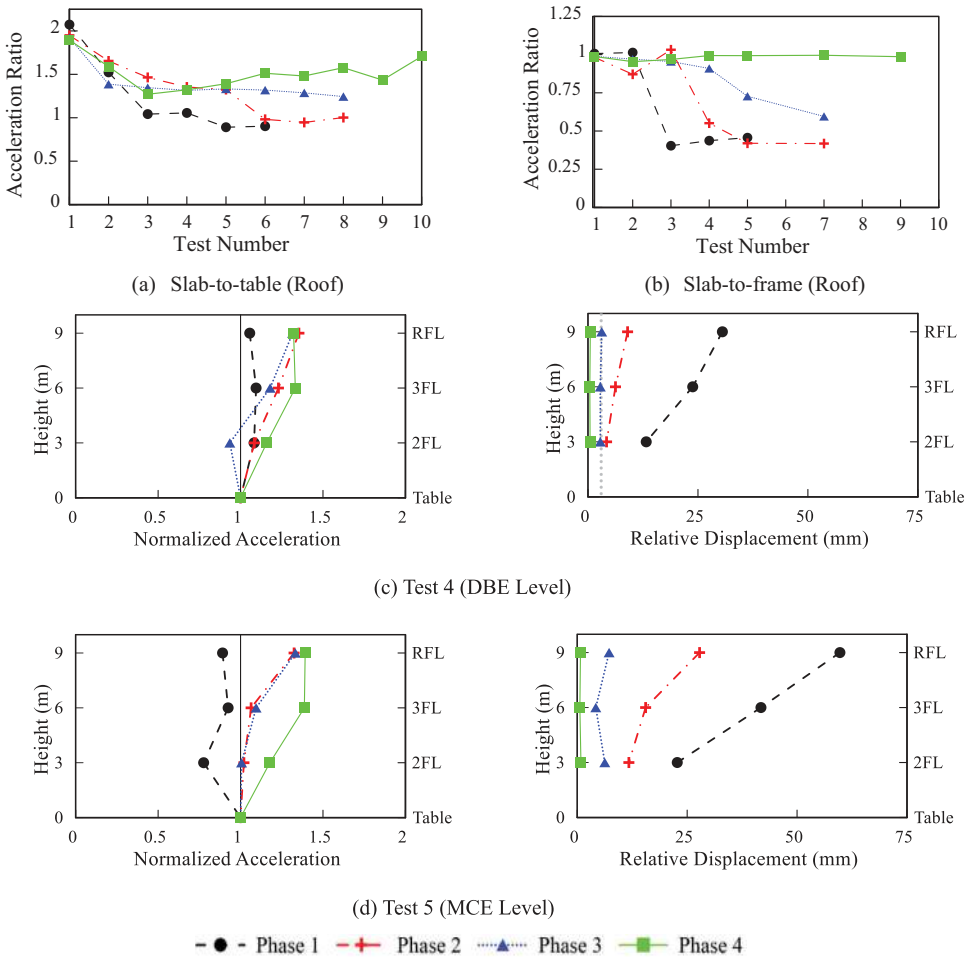


FIGURE 12 | Acceleration and relative displacement of the slab.

to the additional force introduced by the horizontal devices, as expressed in Equation (4). Consequently, slab accelerations were higher in Phases 2 and 3, compared to Phase 1. This is clear when comparing the acceleration ratio up to Test 5 for the different phases (Figure 12a). In Phase 2, Figure 12a shows that although the motion intensity increases from Test 5 to Test 6 (from 0.98 to 1.2 times the MCE level), the total floor acceleration remains effectively constant in Phases 1 and 3. However, from Test 6 to Test 7 (1.2 to 1.6 times the MCE level), this ratio remains constant in Phase 2, suggesting an increase in floor acceleration. This is explained by the large relative displacement observed in Test 7, as shown in Figure 10c, which led to increased force in the spring device alone, assuming that the FD and the frictional behavior of the Teflon remained constant in Phase 2. Figure 12c,d show the slab-to-table acceleration and relative displacement of different floors under the DBE and MCE levels. As shown in Table 4 and Figure 6, Tests 4 and 5 in all four test phases correspond approximately to the seismic intensities of DBE and MCE levels for a frame with a fundamental period of 0.4 s. Note that, except for the roof in Phases 2 and 3, the second- and third-floor accelerations are also reduced compared to those in Phase 4, due to the initiation of slab movement starting at Test 4 (DBE level), as seen in Figure 10c. Greater acceleration reduction and increased slab movement are observed at the MCE level. This behavior is consistent with the design goal of activating the slab movement near the DBE level.

Figure 12b shows the slab acceleration normalized with respect to the frame acceleration at the roof. As expected, the acceleration ratio in Phase 4 is about a value of 1.0 in all tests. In Phase 1, the slab acceleration is about 0.5 times the frame acceleration when the slab sliding is activated. In Phases 2 and 3, the acceleration ratio decreases from Test 4 with the increase of slab sliding; a larger relative displacement of the slab in Phase 2 than in Phase 3 (Figure 10c) results in a larger acceleration reduction. In Test 7, the acceleration ratio is 0.4 and 0.6 in Phases 2 and 3, respectively.

5.2 | Energy Dissipation of Sliding Slab and Frame

The earthquake's input energy to a conventional frame is dissipated by the beams, columns, and braces. For the frame specimen with a sliding slab, the movement of the slab can also dissipate energy in addition to the frame members. The input energy, E_{input}, for a conventional frame is computed based on the work of Uang and Bertero [39]:

$$E_{input} = \int \sum_i \left(m_i \ddot{u}_i \right) du_g, \; i = \text{2FL, 3FL, RFL} \tag{8}$$

where m_i is the mass of the i-th floor, $\ddot{u}_i$ is the absolute acceleration at the i-th floor, and u_g is the shaking table displacement. Since the slab is connected to the test frame with horizontal

10969845, 2025, 15, Downloaded from https://onlinelibrary.wiley.com/doi/10.1002/eqe.70053 by Georgios Tsampras - University Of California , Wiley Online Library on [07/11/2026]. See the Terms and Conditions (https://onlinelibrary.wiley.com/terms-and-conditions) on Wiley Online Library for rules of use; OA articles are governed by the applicable Creative Commons License

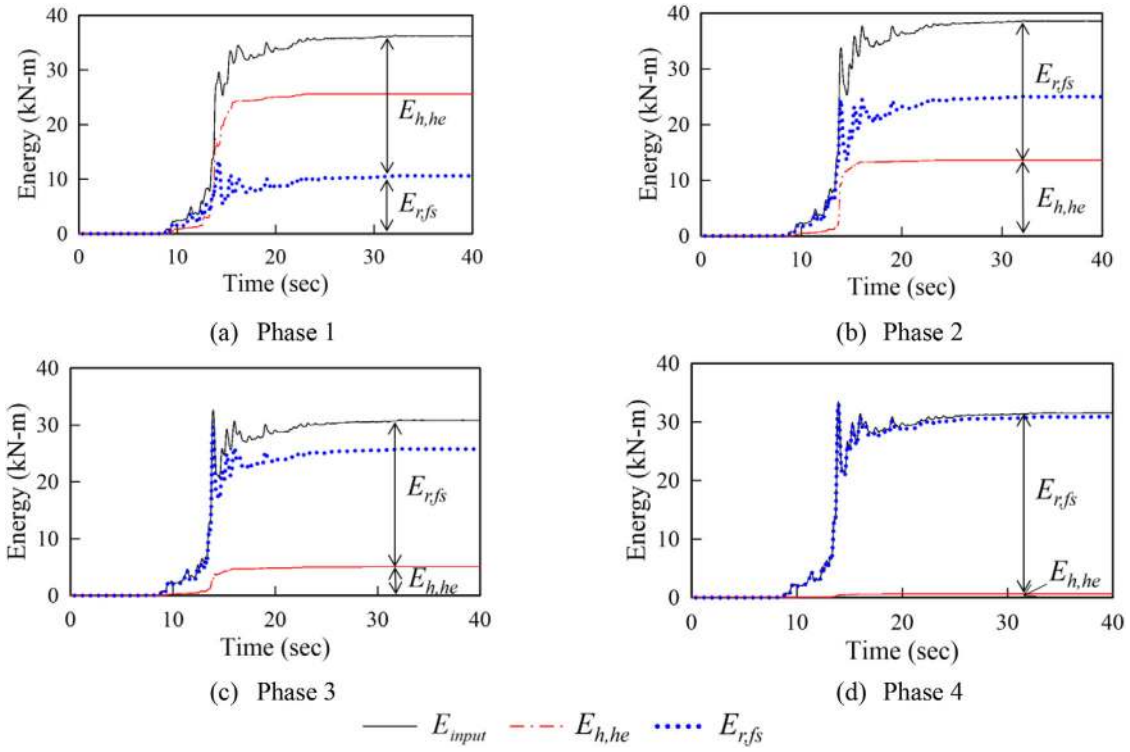


FIGURE 13 | Energy time histories in Test 5 of all phases.

devices, the slab and the frame have different accelerations, as shown in Figure 11. The total input energy is modified as follows:

$$E_{input} = \sum_i \int \left(m_{f,i}\ddot{u}_{f,i} + m_{s,i}\ddot{u}_{s,i} \right) du_g, \; i = 2\text{FL}, \; 3\text{FL}, \; \text{RFL} \tag{9}$$

$$= E_{h,he} + E_{r,fs} \tag{10}$$

where $m_{f,i}$ is the mass of the frame at the i-th floor, $\ddot{u}_{f,i}$ is the absolute acceleration of the frame at the i-th floor, $m_{s,i}$ is the slab mass of the i-th floor, and $\ddot{u}_{s,i}$ is the absolute acceleration of the slab at the i-th floor. The term, $E_{h,he}$, is the hysteretic energy dissipated by the horizontal elements, which are the SCSD, FD or H-SBRB, and Teflon in contact with the steel beam. The remaining energy, $E_{r,fs}$, includes (1) the kinetic energy, strain energy, and damping energy of the steel frame and slab, and (2) the hysteretic energy dissipated by steel frame members (i.e., beam, column base, and brace). In Phases 2 and 3, the hysteretic energy of the horizontal elements, $E_{h,he}$, is expressed as:

$$E_{h,he} = \sum_i \int \left(F_{SCSD} + F_{device} + F_f \right) du_{rel,i}$$

$$= \sum_i \int F_{in,i} du_{rel,i}, \quad i = 2\text{FL}, \; 3\text{FL}, \text{RFL} \tag{11}$$

The remaining energy, $E_{r,fs}$, is obtained by subtracting $E_{h,he}$ from E_{input}.

Figure 13 shows the cumulative energy histories in Test 5 (MCE level) of all phases. Since the frame is installed with different energy dissipation devices, the shaking table motion intensity and the corresponding E_{input} vary slightly for the same test number in different phases. The total input energy, E_{input}, varies between 30 and 40 kN-m in all phases. $E_{h,he}$ is significantly larger than $E_{r,fs}$ in Phase 1 than other phases due to a larger slab relative displacement. In Phases 2 and 3, $E_{r,fs}$ is larger than $E_{h,he}$ (Figure 13b,c) because the frame reached a roof drift angle of approximately 0.005 rad, resulting in yielding of steel braces and, consequently, a higher contribution from the hysteretic energy of the steel frame. In contrast, the slab with energy dissipation devices has lower movement, as shown in Figure 10c. As expected in Phase 4, the slab sliding is minimal so $E_{h,he}$ is negligible compared to $E_{r,fs}$. Figure 14 shows the maximum $E_{h,he}$ and $E_{r,fs}$ in different tests of four phases. The bar chart is the energy and its value is indicated on the left ordinate. The dashed line represents the ratio of the energy of the horizontal elements, $E_{h,he}$, and the remaining energy, $E_{r,fs}$, with respect to E_{input} in each test, and its value is indicated on the right ordinate. In Phase 1, the contribution of $E_{r,fs}$ to the total energy decreases with the test intensity; the contribution of $E_{h,he}$ starts exceeding that of $E_{r,fs}$ in Test 4 (i.e., DBE level), as observed by the crossing of two dashed lines. In Phases 2 and 3, the $E_{h,he}$ contribution is not as predominant as in Phase 1, but it increases with the increasing test intensity. The sliding slab can still be viewed as one of the energy dissipation mechanism in Phases 2 and 3. The energy, $E_{r,fs}$, accounts for more than 95% of the total input energy in all tests of Phase 4.

5.3 | Column and Brace Response

Beams and columns in the frame remained elastic in the first three phase tests, so the frame response only in Phase 4 is presented here. The first-story column base yielded in Test 9, Phase 4 (1.9 × MCE level). Figure 15a shows the hysteretic response

10969845, 2025, 15, Downloaded from https://onlinelibrary.wiley.com/doi/10.1002/eqe.70053 by Georgios Tsampras - University Of California , Wiley Online Library on [07/11/2026]. See the Terms and Conditions (https://onlinelibrary.wiley.com/terms-and-conditions) on Wiley Online Library for rules of use; OA articles are governed by the applicable Creative Commons License

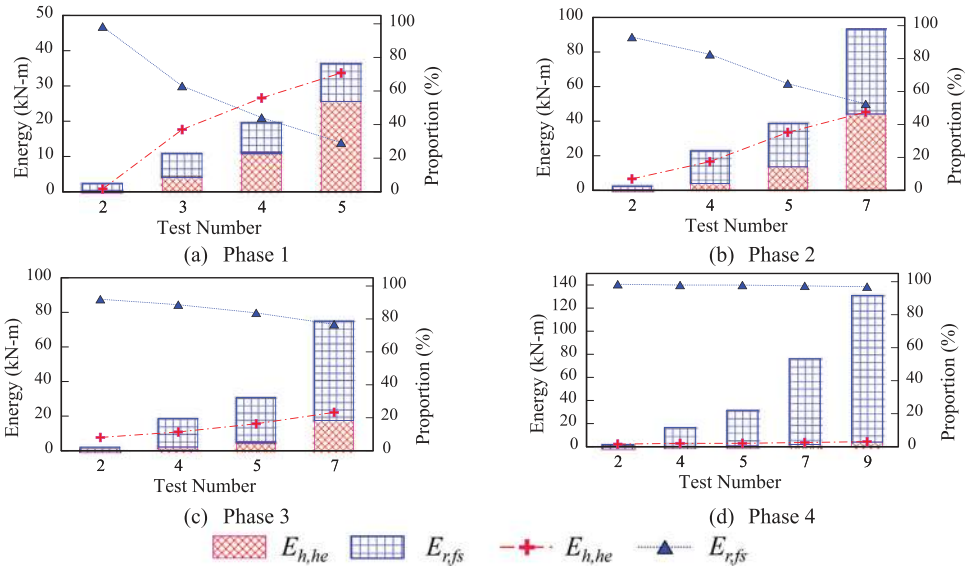


FIGURE 14 | Maximum slab energy and frame energy in tests.

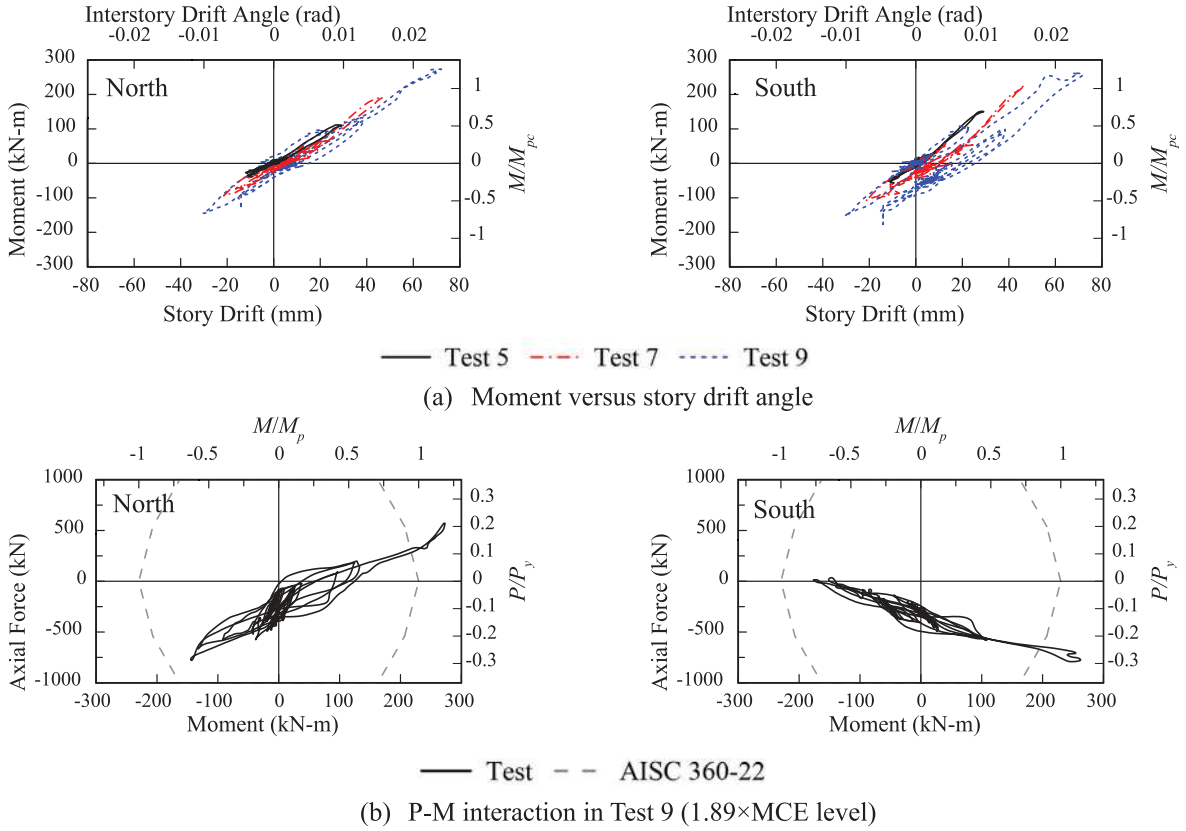


FIGURE 15 | First-story column base response in Phase 4.

of the columns at the base, where moments were computed by measured strains of two flanges along the column height. Two columns exceeded the plastic moment, M_{pc}, in Test 9, with a peak interstory drift angle of 0.024 rad, and Figure 15b shows the P-M interaction of the column based on AISC 360-22 [32]. The column response is within the P-M interaction curve most of the time except for one big pulse motion at $t = 11$ s. Figure 16a,b show photos of the column base after Test 10 (Phase 4), where no local buckling was observed even at the 1.9 × MCE level.

The horizontal component of the diagonal brace force was obtained by subtracting the column shear from the story shear, from which the brace axial force can be determined. The axial displacement of the brace was obtained from displacement

10969845, 2025, 15, Downloaded from https://onlinelibrary.wiley.com/doi/10.1002/eqe.70053 by Georgios Tsampras - University Of California , Wiley Online Library on [07/11/2026]. See the Terms and Conditions (https://onlinelibrary.wiley.com/terms-and-conditions) on Wiley Online Library for rules of use; OA articles are governed by the applicable Creative Commons License

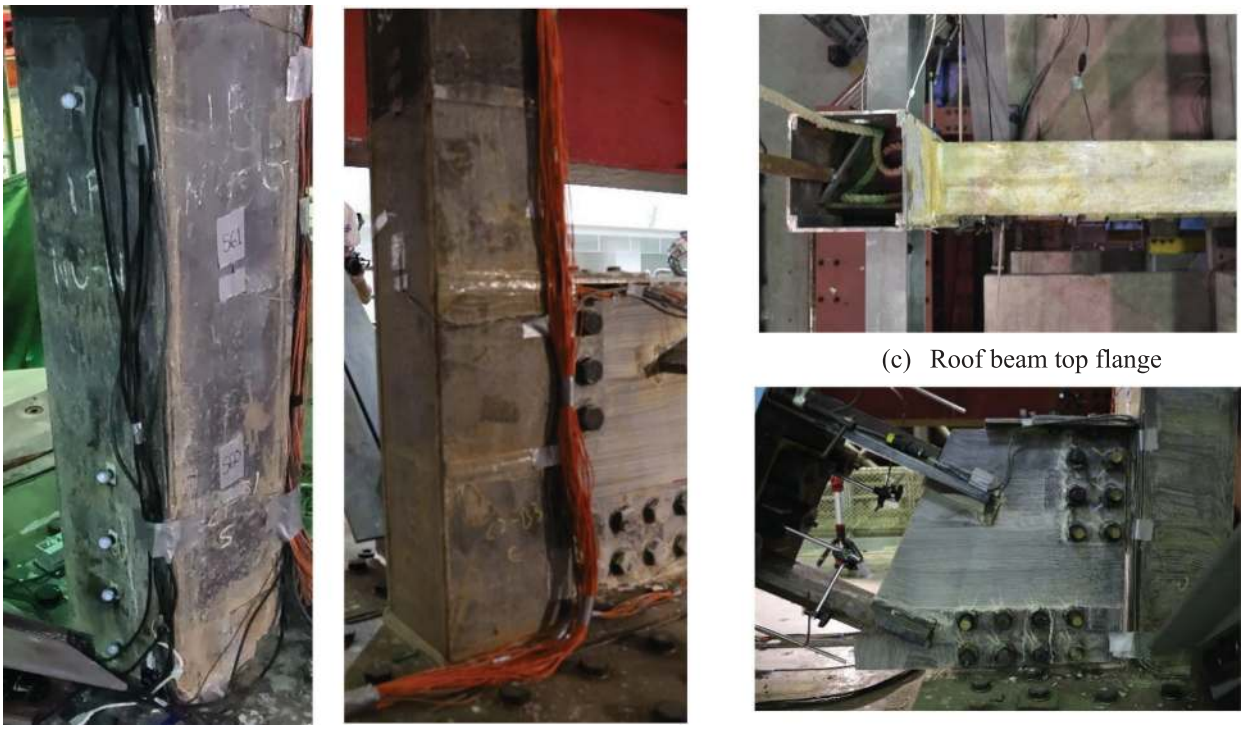


FIGURE 16 | Photos after Test 9 (1.89 × MCE level), Phase 4.

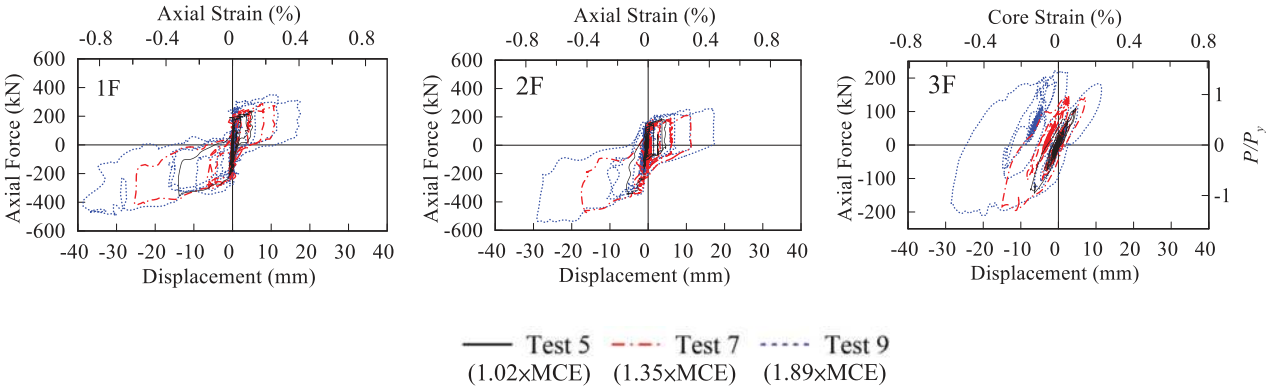


FIGURE 17 | SCB and D-SBRB responses in Phase 4.

transducers positioned at both ends of the brace. Figure 17 shows the hysteretic responses of the two SCBs and one all-steel D-SBRB in Tests 5, 7, and 9 (Phase 4). The SCB shows the expected flag-shaped hysteretic behavior up to Test 9 [10], which minimized the frame residual drift at the end of each test (Figure 7). Figure 16d shows a bolted brace gusset-to-frame connection in the first story, where no yield or bolt slippage were observed throughout the test. The all-steel D-SBRB in the third story also shows a stable hysteresis response as seen in component or frame tests [28–30].

5.4 | Responses of Horizontal Devices

The inertial force, $F_{in,i}$, in Equation (4) was computed by multiplying the floor absolute acceleration by the corresponding mass. The forces in the horizontal energy dissipation device, $F_{device,i}$, and the SCSD, $F_{SCSD,i}$, could not be computed directly or readily measured from the shaking table tests. Instead, they were obtained from single-component tests conducted after all shaking table tests. Figure 18 shows the test setup for an FD and an H-SBRB, which were removed from the roof of the frame specimen after the Phase 3 test. The energy dissipation device was tested in a 5000 kN universal testing machine. The displacement history imposed on each device was based on the axial displacement history of the device measured during the shake table test. Figure 19a shows the axial force versus displacement response of the device together with the roof inertial force response, where the device force for comparing to the inertial force of the roof was doubled because two devices were used per floor. The SCSD, FD, or H-SBRB performed as expected, and the sum of forces from the SCDS and energy dissipation device (i.e., FD or H-SBRB) is close to the floor inertial force. Note that the initial yield force of the H-SBRB is close to the friction force of FD, but the axial force of the H-SBRB increases in the nonlinear strain-hardening state,

10969845, 2025, 15, Downloaded from https://onlinelibrary.wiley.com/doi/10.1002/eqe.70053 by Georgios Tsampras - University Of California , Wiley Online Library on [07/11/2026]. See the Terms and Conditions (https://onlinelibrary.wiley.com/terms-and-conditions) on Wiley Online Library for rules of use; OA articles are governed by the applicable Creative Commons License



(a) FD (b) H-SBRB

FIGURE 18 | Test setup for the horizontal energy dissipating device.

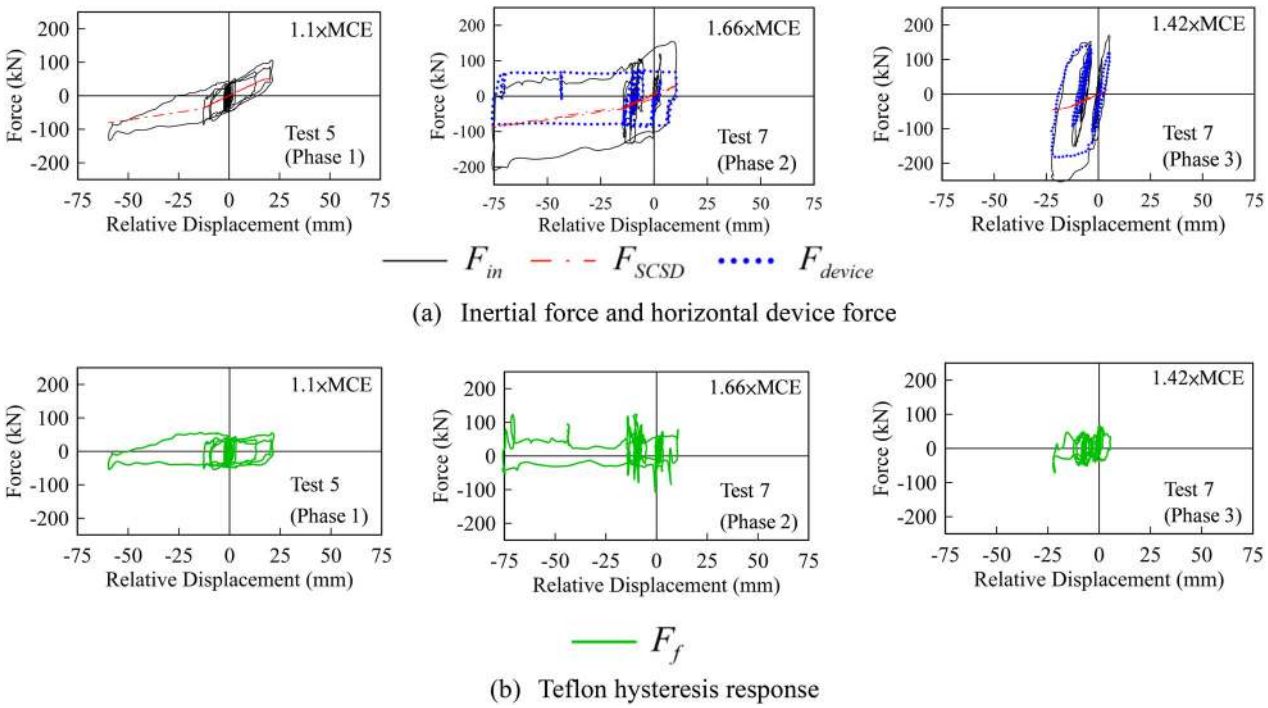


FIGURE 19 | Force versus relative displacement response of the roof horizontal devices and Teflon.

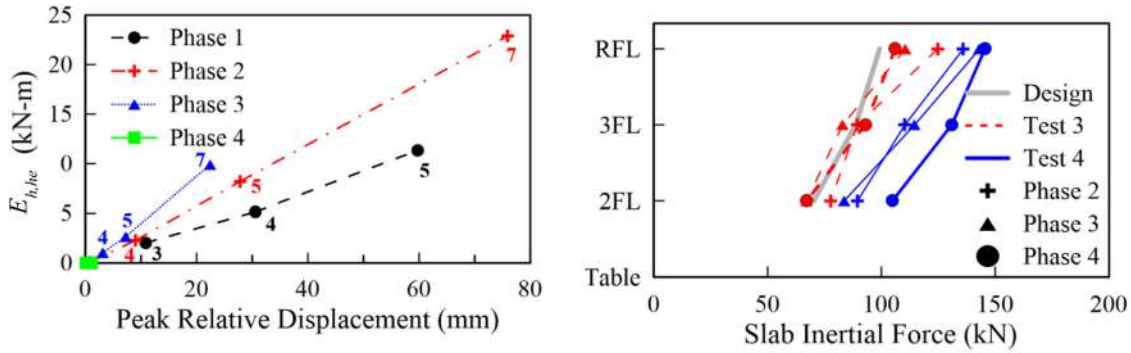
unlike the rectangular hysteretic response of the FD. Figure 19b shows the Teflon hysteresis response, computed by subtracting the forces of the horizontal devices (SCSD, FD, or H-SBRB) from the inertial force. The frictional response of Teflon due to the slab sliding over the steel beams provides additional energy dissipation to the sliding system.

5.5 | Diaphragm Force

Figure 20a presents the relationship between the hysteretic energy of horizontal elements, $E_{h,he}$, and the peak relative displacement, u_{rel}, labeled with the corresponding test number. The slope of the relationship represents the energy dissipated per unit peak relative displacement, which indicates the efficiency of the slab's energy dissipation. The slab in Phase 1 has the lowest energy dissipation efficiency because no energy dissipating device is used, while in Phase 3, it has the highest energy dissipation efficiency. However, in Phase 2, the slab dissipates a greater amount of energy due to a larger relative displacement (i.e., 78 mm). The slope in Phase 3 is 28% higher than that in Phase 2 due to the increased force per unit relative displacement of the H-SBRB in the strain-hardening state. When comparing only Test 5 results (i.e., MCE level) across different phases, the slab dissipates much more energy in Phases 1 and 2 than in Phase 3, indicating small slab movement when installed with H-SBRB, as opposed to the FD.

Figure 20b shows the design diaphragm force, F_{px}, along with the inertial forces, measured in Tests 3 and 4 of Phases 2–4. In Tests 3, the inertial force distribution pattern in Phase 4 (i.e., "rigidly-connected" slab connection) is similar to the diaphragm force pattern, F_{px}, in ASCE 7-22 [34], as in a typical frame structure without slab sliding. In Test 4, close to the DBE level (see Table 4), the inertial force at each floor is larger than the code value, indicating that Equation (5) from ASCE 7-22 significantly

10969845, 2025, 15, Downloaded from https://onlinelibrary.wiley.com/doi/10.1002/eqe.70053 by Georgios Tsampras - University Of California , Wiley Online Library on [07/11/2026]. See the Terms and Conditions (https://onlinelibrary.wiley.com/terms-and-conditions) on Wiley Online Library for rules of use; OA articles are governed by the applicable Creative Commons License



(a) $E_{h,he}$ versus peak u_{rel} at RFL

(b) Diaphragm design force and inertial force

FIGURE 20 | Sliding slab and inertial force distribution.

underestimates the slab force for a "rigidly-connected" slab-to-frame system (Phase 4). Moreover, the floor inertial force reduces in Phases 2 and 3 due to slab sliding when compared to the Phase 4 test.

6 | Conclusions

The research aimed to evaluate the effect of a sliding slab on a three-story, steel re-centering braced frame in shaking table tests [40]. Four phases with 32 tests were conducted on the frame using a ground motion record obtained from the EYUL-EW station during the 2022 Guanshan and Chihshang Earthquake in Taiwan [36]. In the first three phases, the slab is decoupled from the steel frame by using Teflon sheets at all precast concrete slab and beam interfaces to minimize friction. Different horizontal energy dissipation devices are used in the first three phases, which include the SCSD in Phase 1, the FD in parallel with the SCDS in Phase 2, and the all-steel sandwiched buckling-restrained brace (H-SBRB) in parallel with the SCDS in Phase 3. A "rigid" connection between the frame and slab is provided in Phase 4 to simulate a typical steel frame construction. Two compact-only built-up box columns, which violate the highly and moderately ductile b/t requirements in AISC 341-22 [27], are used in the frame to study their seismic response up to an earthquake intensity of two times MCE level. The main findings are summarized below.

1. The frame specimen with only SCSDs in Phase 1 exhibited the largest seismic response reduction among all phases, reducing the steel frame roof drift by 58% (Figure 8a) and the base shear by 39% (Figure 8d) in Test 5 (MCE level) when compared to the Phase 4 test. The SCSD effectively minimized the residual relative displacement between the slab and the frame after the slab moved 61 mm, with a residual displacement of 2 mm at the MCE level (Figure 10c,d). However, the SCSD connected between the slab and the frame led to excessive slab sliding below the DBE level (Test 4). It is recommended to incorporate additional energy dissipation devices together with SCSDs to limit the slab/frame relative displacement during a small earthquake.
2. A significant reduction in the slab acceleration was clearly observed in Phase 2 and 3 tests, compared to the Phase 4 test (Figures 11 and 12), which started at DBE level due to the slab movement. More floor acceleration was reduced at MCE (Test 5) or higher earthquake intensity levels. This led to a reduction of roof frame drift of 23% and 18%, and a base shear reduction of 15% and 5% in Phases 2 and 3, respectively. The sliding slab, equipped with SCSDs in parallel with horizontal energy dissipation devices (i.e., FD or H-SBRB), reduced the seismic force and base shear on the frame compared to the Phase 4 test (see Figure 8c,d at MCE level). Test results verified that the strategy, incorporating a sliding slab with force-limiting devices, reduces inelastic demands and drift in the primary frame, thereby limiting damage to nonstructural components and supporting the objective of achieving functional recovery after a major earthquake.
3. The frame specimen dissipated much less energy than the sliding slab in Phase 1 due to a larger slab relative displacement. In Phases 2 and 3, the steel frame became the primary source of energy dissipation rather than the slab in Phase 1 (Figure 13). Nonetheless, the proportion of energy contributed by the sliding slab increased relative to the total input energy as the test intensity increased, particularly after the DBE level (Figure 14b,c). The slab dissipated less energy due to the additional force resistance introduced by the horizontal energy dissipation device to limit slab sliding, indicating an energy trade-off between the frame and the sliding slab during a large earthquake.
4. The frame specimen in Test 9 (1.9 × MCE level) of Phase 4 experienced 3.4 times the design base shear and reached a maximum interstory drift angle of 0.024 rad (Figure 15a). The column's plastic moment was exceeded at the base, with a maximum instantaneous axial force of $0.3P_y$. No local buckling was observed after testing (Figure 16a,b), and no strength degradation was observed from the moment of hysteretic response. The residual displacement of the frame specimen with the SCB was very small even at an earthquake intensity close to two times the MCE level (Figures 7d and 17), much less than the repair limits in [34, 38]. The SCB and all-steel sandwiched buckling-retrained brace in the frame specimen performed as expected from single-component tests [10, 28]. The test also indicates that the highly ductile b/t requirement ($\lambda_{hd} = 12.5$) for built-up box columns in a steel braced frame, as per AISC 341-22 [27], is overly conservative

10969845, 2025, 15, Downloaded from https://onlinelibrary.wiley.com/doi/10.1002/eqe.70053 by Georgios Tsampras - University Of California , Wiley Online Library on [07/11/2026]. See the Terms and Conditions (https://onlinelibrary.wiley.com/terms-and-conditions) on Wiley Online Library for rules of use; OA articles are governed by the applicable Creative Commons License

for the columns (i.e., $b/t = 27.4$ in this study), where the initial axial force is $0.1P_y$ with an axial load variation up to $0.2P_y$.

5. The design force of the horizontal energy dissipation device was based on Equation (5) in ASCE 7-22 [34], which closely matched the inertial force obtained in Test 3 (i.e., a peak table acceleration of 0.19 g). Then, the slab sliding was activated in Test 4 of Phases 2 and 3 with a peak table acceleration of 0.22–0.25 g (DBE level). The tests also showed that the floor inertial force measured at the DBE level in Phase 4 (i.e., "rigidly-connected" slab) was significantly higher than the value predicted by Equation (5) in ASCE 7-22.

Acknowledgments

This research was supported by the National Science and Technology Council under the project number NSTC 112-2625-M-002-019, Taiwan and the 2022 Innovative Project of National Applied Research Laboratories. The technical support from the laboratory staff at NCREE is appreciated.

Data Availability Statement

The data that support the findings of this study are available from the corresponding author upon reasonable request.

References

1. C. Christopoulos, R. Tremblay, H.-J. Kim, and M. Lacerte, "Self-Centering Energy Dissipative Bracing System for the Seismic Resistance of Structures: Development and Validation," *Journal of Structural Engineering* 134, no. 1 (2008): 96–107.

2. C. C. Chou, Y. C. Chen, D. H. Pham, and V. M. Truong, "Steel Braced Frames with Dual-Core SCBs and Sandwiched BRBs: Mechanics, Modeling and Seismic Demands," *Engineering Structures* 72 (2014): 26–40.

3. C. C. Chou and P. T. Chung, "Development of Cross-Anchored Dual-Core Self-Centering Braces for Seismic Resistance," *Journal of Constructional Steel Research* 101 (2014): 19–32.

4. J. Erochko, C. Christopoulos, and R. Tremblay, "Design, Testing, and Detailed Component Modeling of a High-Capacity Self-Centering Energy Dissipative Brace," *Journal of Structural Engineering* 141, no. 8 (2015): 04014193.

5. C. C. Chou and Y. C. Chen, "Development of Steel Dual-Core Self-Centering Braces: Quasi-Static Cyclic Tests and Finite Element Analyses," *Earthquake Spectra* 31, no. 1 (2015): 247–272.

6. J. Li and L. H. Xu, "Seismic Responses and Damage Control of Long-Span Continuous Rigid-Frame Bridges Considering the Longitudinal Pounding Effect Under Strong Ground Motions," *Journal of Bridge Engineering* 28, no. 2 (2023): 04022140, https://doi.org/10.1061/JBENF2.BEENG-5871.

7. P. Chen, L. H. Xu, and X. Xie, "Enhanced Design and Experimental Investigation of Disc Spring-Based Self-Centering Buckling-Restrained Braces with a Compounded Combination Mode," *Earthquake Engineering & Structural Dynamics* 52 (2023): 3053–3073, https://doi.org/10.1002/eqe.3912.

8. H. Jiang, L. H. Xu, X. Xie, and P. Chen, "Seismic Behavior of Double Activation Self-Centering Brace and Braced Structures," *Journal of Structural Engineering* 149, no. 7 (2023): 04023082.

9. C. C. Chou, J. F. Hon, and B. Y. Bai, "Development of a Compression-Only Self-Centering Brace with Buckling-Restrained Bars for Energy Dissipation," *Journal of Structural Engineering* 150, no. 9 (2024): 04024124.

10. C. C. Chou and L. Y. Huang, "Mechanics and Validation Tests of a Post-Tensioned Self-Centering Brace with Adjusted Stiffness and Deformation Capacities Using Disc Springs," *Thin-Walled Structures* 195 (2024): 111430.

11. D. Mar and S. Tipping, "Story Isolation: A New High-Performance Seismic Technology," in *9th US-Japan Workshop on the Improvement of Structural Design and Construction Practices* (Victoria, Canada, 2000).

12. R. Villaverde, "Roof Isolation System to Reduce the Seismic Response of Buildings: A Preliminary Assessment," *Earthquake Spectra* 14, no. 3 (1998): 521–532.

13. R. Villaverde, "Aseismic Roof Isolation System: Feasibility Study with 13-Story Building," *Journal of Structural Engineering* 128, no. 2 (2002): 188–196.

14. S. Cui, M. Bruneau, and A. Kasalanati, "Behavior of Bidirectional Spring Unit in Isolated Floor Systems," *Journal of Structural Engineering* 136, no. 8 (2010): 944–952.

15. S. Cui, M. Bruneau, and A. Kasalanati, "Seismic Response Case Study of Isolated Floor System Having Special Biaxial Spring Units," *Journal of Structural Engineering* 142, no. 12 (2016): 05016002.

16. S. Liu and G. P. Warn, "Seismic Performance and Sensitivity of Floor Isolation Systems in Steel Plate Shear Wall Structures," *Engineering Structures* 42 (2012): 115–126.

17. H. Anajafi and R. A. Medina, "Robust Design of a Multi-Floor Isolation System," *Structural Control and Health Monitoring* 25, no. 4 (2018): e2130.

18. L. Casagrande, E. Villa, A. Nespoli, A. Occhiuzzi, A. Bonati, and F. Auricchio, "Innovative Dampers as Floor Isolation Systems for Seismically-Retrofit Multi-Story Critical Facilities," *Engineering Structures* 201 (2019): 109772.

19. Y. Xiang and Y. Koetaka, "Structural Feasibility of Incorporating the LVEM-Isolated Floor in the First Story of a Two-Story Steel Frame," *Engineering Structures* 199 (2019): 109686.

20. G. Tsampras, R. Sause, D. Zhang, et al., "Development of Deformable Connection for Earthquake-Resistant Buildings to Reduce Floor Accelerations and Force Responses," *Earthquake Engineering & Structural Dynamics* 45, no. 9 (2016): 1473–1494.

21. G. Tsampras, R. Sause, R. B. Fleischman, and J. I. Restrepo, "Experimental Study of Deformable Connection Consisting of Buckling-Restrained Brace and Rubber Bearings to Connect Floor System to Lateral Force-Resisting System," *Earthquake Engineering & Structural Dynamics* 46, no. 8 (2017): 1287–1305.

22. G. Tsampras, R. Sause, R. B. Fleischman, and J. I. Restrepo, "Experimental Study of Deformable Connection Consisting of Friction Device and Rubber Bearings to Connect Floor System to Lateral Force-Resisting System," *Earthquake Engineering & Structural Dynamics* (2017), https://doi.org/10.1002/eqe.3004.

23. Z. Zhang, R. B. Fleischman, J. I. Restrepo, et al., "Shake-Table Test Performance of an Inertial Force-limiting Floor Anchorage System," *Earthquake Engineering & Structural Dynamics* 47, no. 10 (2018): 1987–2011.

24. M. Paronesso and D. G. Lignos, "Seismic Design and Performance of Steel Concentrically Braced Frame Buildings with Dissipative Floor Connectors," *Earthquake Engineering & Structural Dynamics* 51, no. 15 (2022): 3505–3525.

25. C. C. Chou, H. Z. Lin, A. Córdova, et al., "Earthquake Simulator Testing of a Three-Story Steel Building for Evaluating Built-Up Box Column Performance and Effect of Sliding Slab," *Earthquake Engineering and Structural Dynamics* 53, no. 9 (2024): 2637–2655.

26. A. Córdova, C. C. Chou, C. J. Wu, G. Tsampras, C. M. Uang, and S. H. Chao, "Modeling and Seismic Response of a Three-Story Steel Building with Sliding Slabs in Earthquake Motions," *Earthquake Engineering and Structural Dynamics* 54, no. 3 (2024): 1101–1121.

27. AISC, *Seismic Provisions for Structural Steel Buildings*, ANSI/AISC 341-22 (American Institute of Steel Construction, 2022).

10969845, 2025, 15, Downloaded from https://onlinelibrary.wiley.com/doi/10.1002/eqe.70053 by Georgios Tsampras - University Of California , Wiley Online Library on [07/11/2026]. See the Terms and Conditions (https://onlinelibrary.wiley.com/terms-and-conditions) on Wiley Online Library for rules of use; OA articles are governed by the applicable Creative Commons License

28. C. C. Chou and S. Y. Chen, "Subassemblage Tests and Finite Element Analyses of Sandwiched Buckling-Restrained Braces," *Engineering Structures* 32, no. 8 (2010): 2108–2121.

29. D. H. Pham and C. C. Chou, "Strong-Axis Instability of Sandwiched Buckling Restrained Braces in a Steel Two-Story X-BRBF: Seismic Tests and Finite Element Analyses," *Thin-Walled Structures* 157 (2020): 107011.

30. C. C. Chou and M. H. Tam, "Cyclic Testing of Two-Story Steel BRBFs for Evaluating Performance of Moderately Ductile Built-Up Box Columns Under Varying Axial Load," *Journal of Structural Engineering* 151, no. 5 (2025): 04025047, https://doi.org/10.1061/JSENDH.STENG-14074.

31. Taiwan Code. *Design and Technique Specifications of Steel Structures for Buildings* (Construction and Planning Agency, 2010).

32. ANSI/AISC 360-22. *Specification for Structural Steel Buildings* (American Institute of Steel Construction, 2022).

33. L. Y. Huang, "Research on an Adjusted-Stiffness Self-Centering Brace and a Slab Self-Centering Disc Spring Device," (PhD diss., *Thesis Advisor: Chou, C. C.*, Dept. of Civil Engineering, National Taiwan University, Taipei, Taiwan in Chinese, 2024).

34. ASCE, *Minimum Design Loads for Buildings and Other Structures*, ASCE/SEI 7-22 (American Society of Civil Engineers, 2022).

35. Schnorr, *Handbook for Disc Springs* (Schnorr Corporation, 2003).

36. C. M. Lin, Y. W. Chang, C. C. Chou, et al., "Reconnaissance of the 2022 Guanshan and Chihshang Earthquakes in Eastern Taiwan," *Earthquake Spectra* (2023), https://doi.org/10.1177/87552930231209102.

37. E. Mrabet, M. Abdelghani, and N. B. Kahla, "A New Criterion for the Stabilization Diagram Used with Stochastic Subspace Identification Methods: An Application to an Aircraft Skeleton," *Shock and Vibration* 2014 (2014): 1–8.

38. FEMA, *Seismic Performance Assessment of Buildings*. FEMA P-58 (FEMA, 2012).

39. C. M. Uang and V. V. Bertero, "Evaluation of Seismic Energy in Structures," *Earthquake Engineering and Structural Dynamics* 19 (1990): 77–90.

40. C. J. Wu, "Shaking Table Tests of a Novel Full-Scale Three-Story Steel Self-Centering Braced Frame with Sliding Slabs," (PhD diss., *Thesis Advisor: Chou, C. C.*, Dept. of Civil Engineering, National Taiwan University, Taipei, Taiwan (in Chinese), 2024).

10969845, 2025, 15, Downloaded from https://onlinelibrary.wiley.com/doi/10.1002/eqe.70053 by Georgios Tsampras - University Of California , Wiley Online Library on [07/11/2026]. See the Terms and Conditions (https://onlinelibrary.wiley.com/terms-and-conditions) on Wiley Online Library for rules of use; OA articles are governed by the applicable Creative Commons License